

**Comprehensive Exam Write-up: Ocean
Circulation Modeling using Adaptive Wavelet
Methods**

by

Shanon M. Reckinger

B.A., Mathematics, University of St. Thomas, 2006

B.S., ME, University of St. Thomas, 2006

A thesis submitted to the
Faculty of the Graduate School of the
University of Colorado in partial fulfillment
of the requirements for the degree of
Doctor of Philosophy
Department of Mechanical Engineering

2010

This thesis entitled:
Comprehensive Exam Write-up: Ocean Circulation Modeling using Adaptive Wavelet
Methods
written by Shanon M. Reckinger
has been approved for the Department of Mechanical Engineering

Prof. Oleg V. Vasilyev

Prof. David R. Kassoy

Prof. Olivier Desjardins

Prof. Baylor Fox-Kemper

Prof. Daven Henze

Date _____

The final copy of this thesis has been examined by the signatories, and we find that
both the content and the form meet acceptable presentation standards of scholarly
work in the above mentioned discipline.

Reckinger, Shanon M. (Ph.D., Mechanical Engineering)

Comprehensive Exam Write-up: Ocean Circulation Modeling using Adaptive Wavelet
Methods

Thesis directed by Prof. Oleg V. Vasilyev

This work applies the adaptive wavelet collocation methodology to various sets of equations that govern ocean, with the goal of being able to more accurately predict global ocean circulation. This work also improves the representation of continental topology and bottom bathymetry for use in ocean circulation models through an extension of the Brinkman penalization method. Due to the complicated geometry inherent in ocean boundaries, the stair-step representation used in the majority of current global ocean circulation models causes accuracy and stability problems. Brinkman penalization is a numerical technique used to enforce no slip boundary conditions through the addition of a term to the governing equations. When coupled with the Adaptive Wavelet Collocation Method, which solves the penalized equations on a temporally and spatially varying mesh, the flow near the boundary can be well defined for less computational cost.

Contents

Chapter

1	Introduction	1
1.1	Motivation and Objective	1
1.2	Methodology	2
1.2.1	A Brinkman Penalization Method	3
1.2.2	Adaptive Wavelet Collocation Method	4
1.3	Organization	4
2	Background	6
2.1	Overview of Physical Ocean Dynamics	6
2.1.1	Geophysical Fluid Mechanics	6
2.1.2	Conceptual Discussion of Ocean Dynamics	8
2.1.3	Ocean Phenomena and Their Scales of Motion	10
2.2	Derivation Governing Equations	14
2.2.1	Primitive Equations (Non-hydrostatic Primitive Equations) . . .	15
2.2.2	Hydrostatic Primitive Equations	19
2.2.3	Shallow Water Model	21
2.3	Ocean Circulation Modeling	23
2.4	Adaptive Wavelet Collocation Method	27
2.5	Brinkman Penalization	31

2.5.1	Methods for Representing Boundaries with Complex Geometries	31
2.5.2	Immersed Boundary Methods for Incompressible Flows	31
2.5.3	Brinkman Penalization for Incompressible Flows	32
2.5.4	Immersed Boundary Methods for Compressible Flows	33
2.5.5	Brinkman Penalization for Compressible Flows	34
3	Shallow Water Model	35
3.1	Physical Model and Governing Equations	35
3.2	Brinkman Penalization Method for Shallow Water Model	35
3.2.1	Wave Speeds	36
3.2.2	Impedance	37
3.2.3	Amplitude and Phase Errors by Asymptotic Analysis	38
3.3	Benchmark Problem I: One Dimensional normal wave	41
3.4	Two-dimensional Wind-driven Double Gyre with Brinkman	43
4	Hydrostatic Primitive Equations	45
4.1	Physical Model and Governing Equations	45
4.2	Extension of Brinkman Penalization	46
5	Non-Hydrostatic Primitive Equations	54
5.1	Physical Model and Governing Equations	55
5.2	Brinkman Penalization for Non-Hydrostatic Equations	55
6	Future Work	57
6.1	Shallow Water Model	57
6.2	Non-hydrostatic Primitive Equations	58
Bibliography		59

Tables**Table**

2.1 Scales of ocean phenomenon	10
2.2 Typical ocean scales	20

Figures

Figure

2.1	Schematic of meridional overturning circulation	9
2.2	Diagram of Ocean Column	10
2.3	Exaggerated schematic of tides	12
2.4	Coastal Upwelling	13
2.5	Mesoscale Eddies	14
2.6	Gulf Stream	14
2.7	Vertical coordinates	25
2.8	Z-coordinate options	25
2.9	1D example of AWCM.	30
2.10	Traditional boundaries vs. Brinkman penalization	33
3.1	Initial conditions for 1D wave	41
3.2	1D wave after complete reflection	42
3.3	Sea surface height convergence plot	42
3.4	Maximum error convergence plot.	43
3.5	2D wind-driven results with Brinkman	44
3.6	2D wind-driven results with Brinkman for variable topography	44
4.1	Schematic of Brinkman Penalization	47
4.2	No slip conditions with and without Brinkman	48

4.3	Error convergence for no slip conditions	48
4.4	Diagram of two formulations of extension of Brinkman to slip conditions	49
4.5	Comparison of two Brinkman methods for slip conditions	51
4.6	Slip conditions, $\kappa = 1$, with and without penalization	51
4.7	Slip conditions, $\kappa = 10$, with and without penalization	52
4.8	Error convergence for slip conditions	52
5.1	Preliminary results of non-hydrostatic form with Brinkman penalization	56

Chapter 1

Introduction

1.1 Motivation and Objective

Ocean circulation is a prototypical “Strongly Coupled Multiscale Phenomenon,” and the computational challenge of modeling it lies in accurately representing the immense range of spatial and temporal scales that interact to produce the intricate and complex behavior that drives low-frequency climate variability. Studies of the variability of our climate system suggest that changes in the meridional overturning circulation (MOC) have the potential to trigger severe climate change events, e.g. [20]. An important component of the MOC is the intricate process of formation of deep water in the North Atlantic, and a popular example of a climate change event is a scenario wherein a weakening of the MOC in the North Atlantic from its present level due to a change in the deep water formation (as, e.g. due to doubled CO₂ levels in the atmosphere) triggers a change to ice-age like conditions[20, 91]. Such studies are presently based on either what are called “box-models” of oceans wherein the global ocean is idealized as a few (typically two or three) interconnected rectangular basins, or more realistic ocean models but at coarse resolutions. While studies using these models have given insights into possible mechanisms for variability of the meridional overturning circulation, the lack of detailed representation of physics in these models makes the significance and applicability of such results to the actual climate system questionable and controversial, e.g. [33].

On the other hand, in comparing either satellite observations or in-situ measurements of circulation or observed tracer transport in the world oceans to the modeled ocean circulation used in climate studies, the pathologically sluggish nature of the modeled circulation is striking; the modeled circulation does not just severely underrepresent mesoscale variability, but also fails to represent the mean circulation reasonably, e.g. [4]. However, studies of ocean circulation on the shorter (annual to decadal) time scale have shown that the global ocean circulation can be modeled realistically using high resolution[78]; an important result coming out of these studies is the major role played by mesoscale eddies. Thus, a systematic study of possible climate change scenarios calls for carrying out a significant number of long-term (centennial to millenial time scale) simulations using realistic models at fairly high resolutions.

Thus, while there is no hope for being able to simulate ocean circulation in full detail in the foreseeable future, the need for reliable and computationally affordable predictions of the large scale aspects of such global circulation is truly pressing: The unprecedented effect of man on the environment mainly through the side-effects of energy consumption patterns is possibly leading us into new climate regimes, leaving the future of the climate system highly uncertain. Given the only climate system that we have, the importance of being able to accurately model such a system becomes apparent.

Since computing power, memory, and time are all scarce resources, the problem of simulating turbulent flows has become one of how to abstract or simplify the complexity of the physics represented in the full governing equations in such a way that the “important” physics of the problem is captured at a lower cost.

1.2 Methodology

The goal of this work is to demonstrate how the adaptive wavelet collocation method can address the computational goals described above. To do this, the wavelet

method is applied to different sets of governing equations for the ocean (shallow water model, hydrostatic primitive equations and non-hydrostatic primitive equations) and verification and testing is done. Additionally, several extensions of Brinkman penalization method were developed and tested to improve representation of continental topology and bottom bathymetry. An introduction to each of these sections of the work is given below.

1.2.1 A Brinkman Penalization Method

Modeling complex boundaries is a pressing issue in the field of ocean modeling. Immersed boundary methods are well known for their efficient implementation of solid boundaries of arbitrary complexity on fixed non-body conformal Cartesian grids. Brinkman penalization, a type of immersed boundary, has been used in many engineering problems to simulate the presence of arbitrarily complex solid obstacles and boundaries. This volume penalization technique is a way to enforce boundary conditions to a specified precision without changing the numerical method or grid used in solving the equations. Its main advantage, when compared to other penalization methods, is that the error can be estimated rigorously and controlled via the penalization parameter [64]. Additionally, it can be shown that the penalized equations converge to the exactly solution in the limit as the penalization parameter tends to zero [8].

Immersed boundary methods have mostly been developed for incompressible flows, but more recently have been extended for compressible flows [70]. Both of these formulations will be used in the following work, as well as further extensions of each. Immersed boundary methods are not as popular in ocean models, however, some models are using them [62].

1.2.2 Adaptive Wavelet Collocation Method

In order to model complex geometries, a non-uniform, adaptive mesh is ideal. For many adaptive models, the main challenge is grid generation. Not only is grid generation difficult, but the process used is often trial and error. It is also very expensive. It is ideal to have the grid follow the structures in the flow in addition to having a grid that adapts to the complicated curves of the continental topology. This requires grid generation at every time step. Two mathematical approaches will be combined to deal with these issues: Brinkman penalization [9] and the adaptive wavelet collocation method [85, 83, 87, 88, 89]. Adaptive wavelet collocation method will efficiently resolve localized flow structures in complicated geometries, while the Brinkman penalization will efficiently implement arbitrarily complex solid boundaries.

The hybrid wavelet collocation - Brinkman penalization method has been investigated for three cases [61, 43, 87, 70]: two dimensional vorticity equation, incompressible Navier-Stokes equations in primitive variable formulation, and compressible Navier-Stokes equations in primitive variable formulation. High Reynolds number flows can be simulated while greatly reducing the number modes and controlling the L_∞ error. The computational cost of the algorithm is independent of the dimensionality of the problem. It is $O(\mathcal{N})$, where \mathcal{N} is the total number of wavelets actually used. The adaptive wavelet collocation method uses second generation wavelets, which allows the order of the method to be variable. Also, the method is easily applied in both two and three dimensions.

1.3 Organization

The rest of this paper is organized as follows. In Chapter 2, the necessary background of ocean circulation modeling and the numerical methods will be covered. For this research, the shallow water model was used as a first step to test out the different

numerical techniques. This work is covered in Chapter 3. Next, testing on the hydrostatic primitive equations was done and this is covered in Chapter 4. The hydrostatic primitive equations were found to not be ideal in working with the wavelet methods, because of the 3D nature of wavelets. Thus, the work switched to begin working with the non-hydrostatic primitive equations. This work is discussed in Chapter 5. Finally, a discussion of future work is found in Chapter 6.

Chapter 2

Background

This chapter provides a background of the various different ideas, methods, models and techniques that contribute to this work. First, an overview of ocean dynamics and ocean models will be reviewed. This will include a conceptual discussion of geophysical ocean dynamics, some comments on the range of scales in the ocean, a complete derivation of the governing equations for oceanic circulation, and finally a review of current ocean models. Next, a description of the numerical method, the adaptive wavelet collocation method, will be provided. Finally, the numerical technique for representing complex boundaries, Brinkman penalization, will be discussed.

2.1 Overview of Physical Ocean Dynamics

To begin, an overview of the physical ocean dynamics involved will be briefly explained. In this section, an introduction to geophysical flows will be provided, then a conceptual discussion of what drives the ocean's movement, and last a description of the immense range of scales in the ocean.

2.1.1 Geophysical Fluid Mechanics

Geophysical flows are a subset of traditional fluid mechanics. When dealing with these large scale flows there are two main effects that strongly influence the dynamics that are not common in all general fluid problems. These two effects are rotation and

stratification.

Everything on Earth is obviously affected by its rotation, however, in most engineering applications it can be neglected because they are occurring on such small scales. There are two forces that result from the earth's rotation: the Coriolis and centrifugal forces. The centrifugal force depends only on the rotation rate (of the earth) and the distance the particle is from the axis of rotation. The force acts as an outward pull. This force is in equilibrium with the gravity force and in most cases the resultant force is just called the gravity force (even though it includes the centrifugal force).

On the other hand, the Coriolis force is the aspect of the rotation of the earth that plays a crucial role in understanding geophysical flows. The main effect of the Coriolis force is that in rapidly rotating, homogenous flows, all the fluid particles will retain vertical alignment. This is known as Taylor curtains. Now, the earth's rotation is not necessarily rapid, nor is the ocean water completely homogenous, however, it does tend towards this idealized behavior. In practice, the Coriolis force is a fictitious force that comes from translating the momentum equations from an inertial frame of reference into a rotating frame of reference.

The second feature of geophysical flows is stratification. Stratification occurs in the ocean due to natural density variations in the fluid. These density variations are mainly a result of temperature and salinity variations within the global ocean. As a result, vertically stacked horizontal layers form with heavy fluids settling to the bottom and lighter to the top. Perturbations occur which disturb this equilibrium. Small perturbations will cause internal waves and large perturbations can cause larger scale convection and mixing that are maintained over time. In many cases (and in this work), the effects of density variations are ignored, in order to focus on the horizontal motion in the ocean such as large scale gyres like the western boundary currents (which are strongly horizontally dominated). [23]

2.1.2 Conceptual Discussion of Ocean Dynamics

The ocean is a complex system affected by all of its various surroundings. However, there are a few mechanisms that can be considered the main driving forces, which include the wind and density variations. Other considerations that affect the ocean include the gravitational pull exerted by the moon and sun (tides), the effect of the atmosphere, sea ice and land, biological effects and marine life, etc . The complexity of the ocean is endless, but even by considering only some of the most dominant forces, it is possible to gain a lot of insight into what is happening.

Wind effects are the main driving force of basin-scale circulations in the upper part of water columns (the mixed layer in Figure 2.2). The ocean water responds to the wind for two reasons. The first is that water has a fairly low viscosity which in turns means it has a very low resistance to the shearing of the air against it. The second is simply that wind pretty consistently blows over the ocean.

The variation in density is the second main driving force in the ocean. These currents happen in the deep waters of the ocean (the abyssal layer in Figure 2.2) and contribute to the vertical movement of the ocean. This circulation is caused first by the formation of deep water masses and then by the movement of these masses. The deep water masses are formed in the polar regions like the North Atlantic and Southern (Antarctic) Oceans. Water at the surface becomes heavy due to cooling from the wind, evaporation at the surface (which removes only pure water, therefore leaving more salty water) and the melting of ice (which also increases salinity). Both increase of temperature and salinity will increase the density of the water. This heavier water will then sink to the bottom of the ocean. Once it hits the bottom, the bathymetry of the ocean floor moves it along. This is called overturning. This process is very slow compared to the motions due to the wind stress. This evolves on the millenial timescale.

The combination of these two drivers make up what is known as the meridional

overtaking circulation, MOC, (also known as the thermohaline circulation or conveyor belt theory). Figure 2.1 is a very simplified schematic of the MOC. It shows the surface currents which are moved by the wind start in the Indian and Pacific Ocean (they are started by a process known as upwelling, which will be discussed later). Then, the deep currents form in the North Atlantic and go south, as was described above. [23]

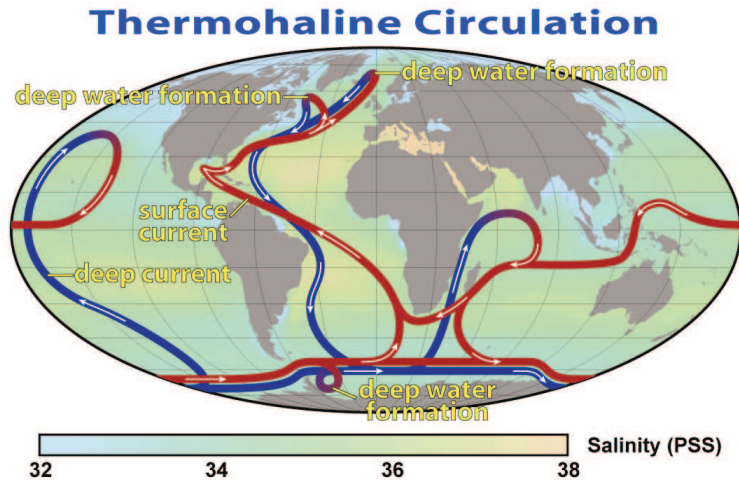


Figure 2.1: Schematic of meridional overturning circulation. The lighter arrows represent surface currents and darker arrows represent deep water currents. [3]

As was mentioned earlier, the ocean can be described in 4 distinct layers. Figure 2.2 shows the four layers: the mixed layer, seasonal thermocline, main thermocline, and the abyssal layer. The top 10 meters of the ocean is called the mixed layer, which gets its name due to the stirring by the wind. The mixed layer is not stratified and therefore density is approximately constant in the vertical direction. The next layer down, the seasonal thermocline, is about 100 m of depth. It is seasonal because the stratification in the seasonal thermocline is erased every winter by convection. Below it, the main thermocline, which varies from about 500-1000 m of depth, is permanently stratified. Below that, is the rest of the ocean, which is called the abyssal layer. The main thermocline and the abyssal layer make up what is known as the ocean interior.

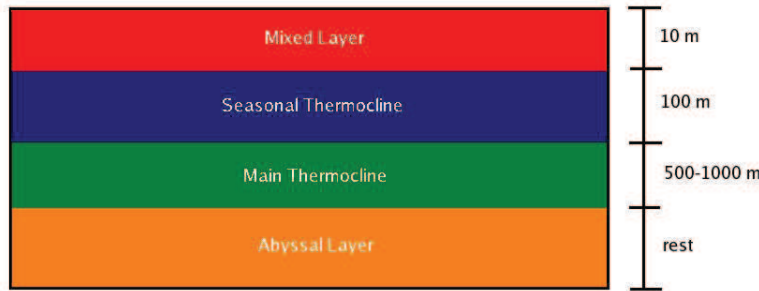


Figure 2.2: Diagram of Ocean Column. Oceans are typically about 5 km deep.

2.1.3 Ocean Phenomena and Their Scales of Motion

One of the difficulties that comes with modeling the ocean is how to incorporate and accurately model the immense range of spatial and temporal scales. The scales range from small scale turbulence that one can see instantaneously when the waves splash up on the beach all the way up the largest scale gyres such as the MOC that cover the entire global ocean and take decades to complete one full cycle. Table 2.1 lists ocean phenomena and the scales of motion associated with them.

Ocean Phenomenon	L	U	T
Microturbulence	1-100 cm	1-10 cm/s	10-100 s
Internal Gravity Waves	1-20 km	0.05-0.5 m/s	min-hrs
Tides	Basin Scale	1-100 m/s	Hours
Coastal Upwelling	1-10 km	0.1-1 m/s	several days
Mesoscale Eddies	5-500 km	0.1-1 m/s	Days to Months
Rossby Waves	Basin Scale	0.5-2 m/s	Months to Years
Major Currents	50-500 km	0.5-2 m/s	Weeks to Seasons
Large-scale Gyres	Basin Scale	0.01-0.1 m/s	Decades and Beyond

Table 2.1: List of Ocean phenomenon and their associated scales. [23]

Microturbulence occurs in the top layer of the ocean (the mixed layer). This is small scale turbulence that occurs due temperature and salinity variations that exist

in the mixed layer being disturbed by the wind. This small scale phenomenon is often modeled using different turbulence parameterization in large ocean general circulation models.

IGravity waves occur both on the surface and on the interior of the ocean. Gravity waves occur at the interface of two fluids with different densities. Surface gravity waves are easily seen in the ocean, especially on the coast. There is a disturbance that causes the water to be displaced upwards. Then, the water that has been raised is heavier than the air around it and it is naturally pulled back down by gravity. The inertia from the vertical velocity that has developed causes the fluid to then penetrate the surface below the equilibrium level. This process repeats causing oscillations along the surface that make up the waves. The waves travel because of the change in the phase of the oscillations from place to place. The same phenomenon happens in the interior of the ocean between two different layers of stratified flow. These waves are slower and longer, since the density difference is much smaller.

Tides are caused by the forces of the moon and the sun acting on the ocean. This causes the rising and falling of the ocean's surface. The distance between the earth and Moon is shorter than the earth and Sun, so the effect of the lunar tides is greater (about twice as great compared to solar tides). As seen in Figure 2.3, a high tide occurs when the moon aligns with a section of the earth. The effect of the moon's gravity pulling on the earth, raises the ocean level in the region nearest the moon. Also, since the earth is being pulled more than the ocean waters on the opposite side of the earth, that side also "rises". The low tide occurs normal to that location in either direction, due to conservation of mass. This explains semidaily or semidiurnal tides, which have two high tides and two low tides each day. However, there are also daily/diurnal tides, which have one low and one high tide per day.

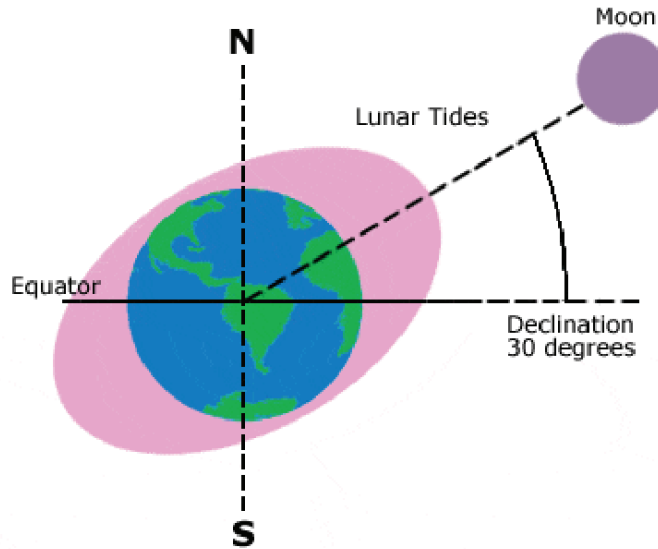


Figure 2.3: Exaggerated schematic of tides. [1]

Upwelling occurs in many ways in the ocean. There is upwelling at the coast, in the interior, near the equator. Upwelling occurs when wind-driven warm, surface water is moved and replaced by deep, cold water. In the Northern Hemisphere, wind-driven currents are diverted to the right of the wind direction (in the Southern Hemisphere they are diverted to the left due to the Coriolis effect). This is known as Ekman transport (a balance of the Coriolis effect and friction). And by the coast, when the wind aligns with the coast on its left, the Ekman transport will move the ocean water to the right (in the Northern Hemisphere), see Figure 2.4. This removes warm, nutrient-lacking water and replaces it with cold, nutrient-rich water. This is especially important for the oceanic food chain and for fisheries.

Eddies have a vast range of scales in the ocean. The eddies of interest in oceanography are referred to as mesoscale eddies and typical values in the ocean are listed in

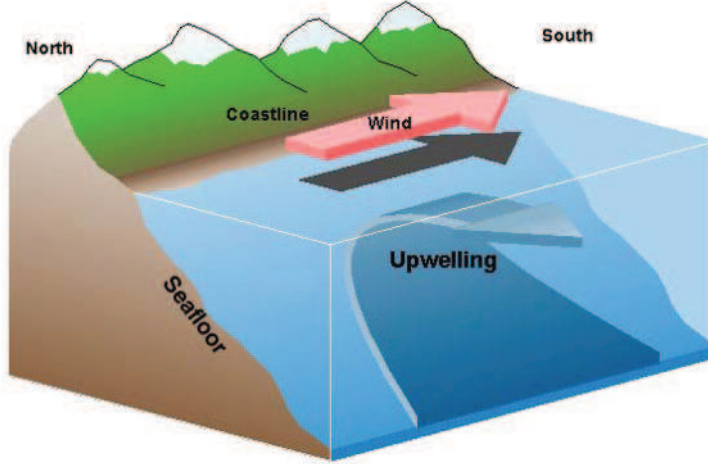


Figure 2.4: A schematic of coastal upwelling. [3]

the Table 2.1. These eddies are typically formed when an ocean current has an instability. This instability eventually grows enough to detach from the large current. These mesoscale eddies are typically formed of water masses that are different from the surrounding water. The circulation in this eddy can be quite fast and of concern for the various operations at sea. It also contributes to the transport of heat within the ocean. Figure 2.5 shows a picture of a mesoscale eddy that formed when the Oyashio and Kuroshio currents collided.

Rossby waves are large scale waves that can affect large ocean currents. These waves are prompted by the meridional change in the Coriolis parameter. These small variations in the Coriolis parameter turn a steady, geostrophic flow into a slowly moving planetary waves. These waves are very difficult to see in the real ocean.

Major ocean currents are large scale circulations. The most well-known example is the Gulf Stream and Kuroshio currents.

Large-scale gyres are referring to circulations like the thermohaline circulation.

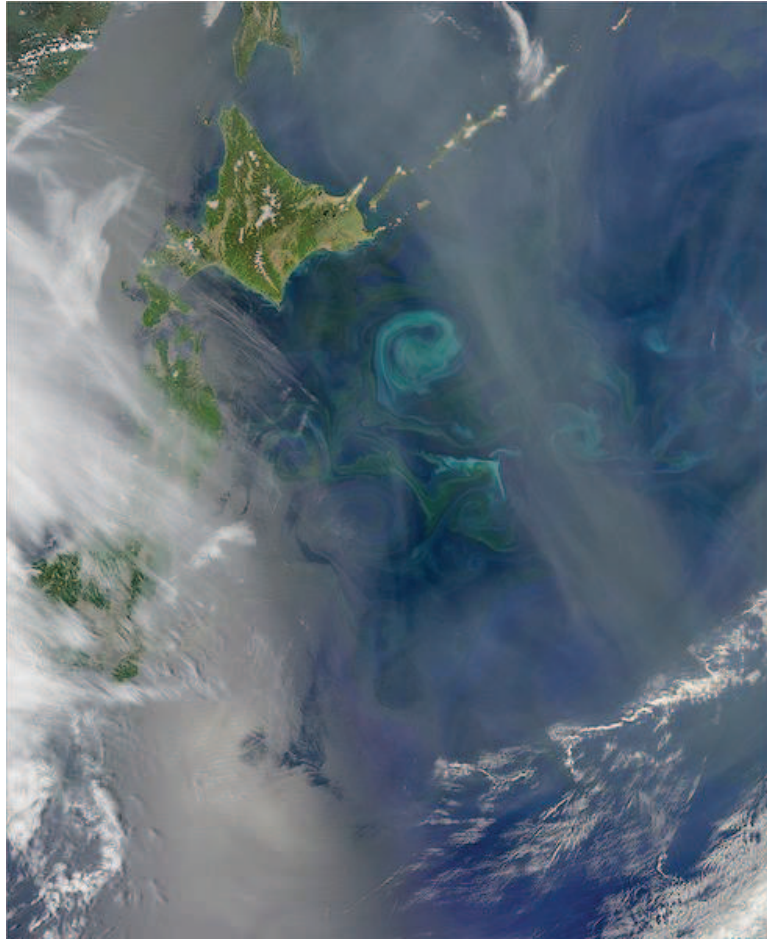


Figure 2.5: The Oyashio and Kuroshio currents collide and a mesoscale eddy is created. In this picture, the phytoplankton become concentrated along the boundary of the eddy and it traces out its motion. [3]

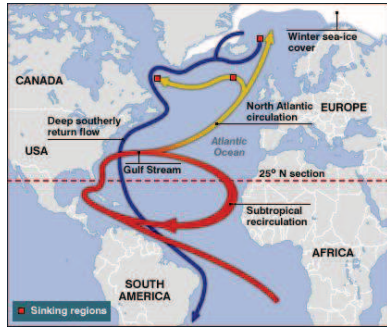


Figure 2.6: Circulation patterns of Gulf Stream. [3]

2.2 Derivation Governing Equations

In this section, a review of three sets of governing equations that describe ocean circulation will be derived. These include the non-hydrostatic primitive equations, the

hydrostatic primitive equations, and shallow water equations, which are in order from most general to the most simplified. [23]

2.2.1 Primitive Equations (Non-hydrostatic Primitive Equations)

As discussed earlier, the difference between geophysical flows versus most engineering flows, is that geophysical flows are affected by the rotation of the earth. Therefore, the governing equations need to incorporate the effect of the earth's rotation. This is done by transforming from the inertial frame of reference where Newton's second law is valid into a rotating frame of reference (of the earth). The result from this transformation is the addition of fictitious forces (Coriolis and centrifugal). The centrifugal force only slightly distorts the earth, because gravity far exceeds the centrifugal force, so it is usually just absorbed into the gravity term. The Coriolis force is not negligible. Taking a time derivative with respect to the inertial framework is equivalent to applying the following operator,

$$\frac{D}{Dt} + 2\boldsymbol{\Omega} \times$$

in a rotating framework (ignoring centrifugal component), where $\boldsymbol{\Omega} = \Omega \cos\phi \mathbf{j} + \Omega \sin\phi \mathbf{k}$ is a vector of the angular rotation of the earth and ϕ is latitude. This results in the following components,

$$\begin{aligned} \frac{du}{dt} &+ 2\Omega \cos(\phi) w - 2\Omega \sin(\phi) v \\ \frac{dv}{dt} &+ 2\Omega \sin(\phi) u \\ \frac{dw}{dt} &- 2\Omega \cos(\phi) u \end{aligned}$$

where often the quantities are defined as, $f = 2\Omega \sin(\phi)$ and $f_* = 2\Omega \cos(\phi)$. The coefficient, f , is the Coriolis parameter and the f_* is the reciprocal Coriolis parameter. The Coriolis parameter is positive in the Northern Hemisphere, negative in the Southern Hemisphere and zero at the equator. The reciprocal Coriolis terms are typically

neglected because they are much smaller than the Coriolis terms. Making these adjustments for a rotating framework to the Navier-Stokes equations for a Newtonian fluid gives,

$$\rho \left(\frac{D\mathbf{u}}{Dt} + f\hat{\mathbf{k}} \times \mathbf{u} \right) = -\nabla P - \rho g\hat{\mathbf{k}} + \mu \nabla^2 \mathbf{u} \quad (2.1)$$

where ρ is density, p is pressure, g is gravitational acceleration, μ is dynamic viscosity. Also, $\frac{D}{Dt}$ is the total derivative. The x-, y- and z- are aligned with the local east, north and up directions. Since the ocean follows the curvature of the earth, a curvilinear coordinate system is the most accurate way to describe the ocean's fluid motion. In that case, Equation 2.1, becomes,

$$\rho \left(\frac{Du}{Dt} - \frac{uv \tan \phi}{r} + \frac{uw}{r} - fv \right) = -\frac{\partial p}{\partial x} + F_x \quad (2.2)$$

$$\rho \left(\frac{Dv}{Dt} + \frac{u^2 \tan \phi}{r} + \frac{uw}{r} + fu \right) = -\frac{\partial p}{\partial y} + F_y \quad (2.3)$$

$$\rho \left(\frac{Dw}{Dt} - \frac{u^2 + v^2}{r} \right) = -\frac{\partial p}{\partial z} - \rho g + F_z \quad (2.4)$$

where, ϕ is latitude and r is the distance to the center of the earth. F_x , F_y , and F_z represent the viscous forces, which are slightly more complicated with the addition of the curvilinear terms. However, in ocean modeling, the length scales are typically restricted to something substantially shorter than the radius of the earth. As a result, all the additional curvilinear terms can be neglected (including those in the viscous term). Thus, Equation 2.1 is used. This assumption can be thought of as the distortion introduced when mapping the curved earth's surface on to a flat plane.

In addition to momentum, the primitive equations include conservation of mass,

$$\frac{\partial \rho}{\partial t} + \nabla \cdot (\rho \mathbf{u}) \quad (2.5)$$

As mentioned before, one of defining features of geophysical flows is the role of stratification. This feature is incorporated through the density field. The density in the ocean

mainly depends on the local temperature, T and salinity, S . The warmer the temperature, the less density the water. And the saltier the water is more dense. Therefore, the equation of state for seawater has some dependence on these two quantities, and as a rough approximation, this could be some linear relationship,

$$\rho = \rho_0[1 - \alpha(T - T_0) + \beta(S - S_0)] \quad (2.6)$$

The constants ρ_0, T_0, S_0 are reference values and α and β are the coefficient of thermal expansion and the coefficient of saline contraction, respectively. Thus, the primitive equations often include some energy equations, mainly in the form of temperature and salinity budgets,

$$\rho C_\nu \frac{dT}{dt} + p(\nabla \cdot \mathbf{u}) = k \nabla^2 T$$

$$\frac{dS}{dt} = \kappa_S \nabla^2 S$$

where C_ν is the heat capacity at constant volume, k is thermal conductivity of seawater, and κ_S is the coefficient of salt diffusion.

In the ocean, the fluid density does not vary greatly. The relative density difference is usually less than 2 % [23]. Therefore, one can write the density in terms of a mean component and a fluctuating component,

$$\rho = \rho_0 + \rho'(x, y, z, t) \quad (2.7)$$

where $\rho' \ll \rho_0$. ρ' is the fluctuation due to stratification and the motion of the fluid, which is small compared to the reference value, ρ_0 . This approximation is called the Boussinesq approximation. If Equation 2.7 is plugged into the continuity equation, Equation 2.5, scale analysis results in the following equation,

$$\nabla \cdot \mathbf{u} = 0 \quad (2.8)$$

This new divergence-free requirement means the volume is conserved. This also eliminates sound waves.

Next, the x and y momentum equation, can be similarly treated. Equations 2.2 and 2.3 have a ρ on the far left side. Ignoring the density variation component (ρ'), the ρ can be replaced by the mean value ρ_0 . This leaves equations 2.9 and 2.10.

$$\frac{Du}{Dt} - fv = -\frac{1}{\rho_0} \frac{\partial p}{\partial x} + \nu \nabla^2 u \quad (2.9)$$

$$\frac{Dv}{Dt} + fu = -\frac{1}{\rho_0} \frac{\partial p}{\partial y} + \nu \nabla^2 v \quad (2.10)$$

The z-momentum equation (Equation 2.4) has a ρ not only on the far left side but also in the product with g on the right side. The left side can be treated the same as the x and y momentum equations. The term ρg accounts for the weight of the fluid which affects the pressure. Writing pressure analogous to how the density was written,

$$p = p_0(z) + p'(x, y, z, t)$$

In the ocean, the pressure is often assumed hydrostatic, which means it only varies with depth. In this case, a less strict assumption is to assume that the reference pressure is hydrostatic,

$$p_0(z) = P_0 - \rho_0 g z \quad (2.11)$$

This means that $\frac{dp_0}{dz} = -\rho_0 g$ and when all is substituted into the Equation 2.4, it reduces to,

$$\frac{Dw}{Dt} = -\frac{1}{\rho_0} \frac{\partial p'}{\partial z} - \frac{\rho' g}{\rho_0} + \nu \nabla^2 w \quad (2.12)$$

The energy equation (Equation 2.2.1) can first be simplified by removing the second term due to the conservation of volume (Equation 2.8). As was done in all the momentum equations, the ρ term on the left side can be replaced with ρ_0 . Then, the energy equation reduces to Equation 2.13.

$$\frac{dT}{dt} = \kappa_T \nabla^2 T \quad (2.13)$$

where $\kappa_T = \frac{k}{\rho_0 C_p}$. Due to the similarity between the temperature equation and the salinity equation (Equation 2.2.1), these two equations can be combined to determine

the evolution of density. However, the simplification can only be made if diffusion is not primarily governed by molecular processes. Therefore, this is only the case on small scales. In general, it can be assumed that in turbulence, diffusion is accomplished by eddies, which mix the salt and heat at equal rates. If this is the case, the terms κ_S and κ_T are equal, thus, $\kappa_S = \kappa_T = \kappa$, also known as the eddy diffusivity. By combining equations 2.2.1, 2.13 and 2.6, the energy equation becomes the density equation (Equation 2.14).

$$\frac{D\rho'}{dt} = \kappa \nabla^2 \rho' \quad (2.14)$$

Now, that there are no longer any terms ρ and p , the primes on ρ' and p' are usually dropped throughout all the equations. The above simplifications make up the Boussinesq approximation.

To summarize, the Boussinesq approximation results in the following non-hydrostatic primitive equations.

$$\frac{D\mathbf{u}}{Dt} + f\hat{\mathbf{k}} \times \mathbf{u} = -\frac{1}{\rho_0} \nabla p + \frac{\rho g}{\rho_0} \hat{\mathbf{k}} + \nu \nabla^2 \mathbf{u} \quad (2.15)$$

$$\nabla \cdot \mathbf{u} = 0 \quad (2.16)$$

$$\frac{D\rho}{dt} = \kappa \nabla^2 \rho \quad (2.17)$$

2.2.2 Hydrostatic Primitive Equations

In most ocean models, the primitive equations are taken one step further by simplifying them with some scale analysis. Table 2.2 summarizes the scales associated with the different ocean variables. As shown in this table, the horizontal lengths and velocities are equivalent in terms of scales, while the vertical is different. The ocean

Variable	Scale	Unit	Value
x	L	m	$10 \text{ km} = 10^4 \text{ m}$
y	L	m	$10 \text{ km} = 10^4 \text{ m}$
z	H	m	100 m
u	U	m/s	$\geq 1 \text{ day} \simeq 9 \times 10^4 \text{ s}$
v	U	m/s	$\geq 1 \text{ day} \simeq 9 \times 10^4 \text{ s}$
w	W	m/s	
p	P	kg/ms^2	
ρ	$\delta\rho$	kg/m^3	0.1 % of ρ_0

Table 2.2: Typical Ocean Scales. [23]

domain is much wider than it is tall. The ocean currents are generally confined to the upper hundred meters, but can extend horizontal in both directions over tens of kilometers. The approximation, then, is that $H \ll L$. The velocity scales will also be different and a look at the continuity equation can give that relationship,

$$\frac{\partial u}{\partial x} + \frac{\partial v}{\partial y} + \frac{\partial w}{\partial z} = 0$$

$$O\left(\frac{U}{L}\right) \quad O\left(\frac{U}{L}\right) \quad O\left(\frac{W}{H}\right)$$

The last term, $\frac{\partial w}{\partial z}$, cannot be greater than the other two terms because that would mean the equation would reduce to $\frac{\partial w}{\partial z} = 0$, which isn't a good approximation for everywhere in the ocean. Since at the bottom of the ocean, the vertical direction of the flow is going to need to converge laterally when it hits the bottom surface. Therefore, the order of the last term needs to be less than or equal to the order of the other two terms. This gives the following relationship:

$$W \leq \frac{H}{L} U$$

and since $H \ll L$, then, $W \ll U$. If a scale analysis using these two simplifications is done on the non-hydrostatic momentum equations (Equation 2.15), the equations reduce to Equations 2.18 - 2.19. This scale analysis simplifies the z momentum equation and it becomes the hydrostatic pressure approximation. Therefore, the equations that result from this scale analysis are known as the hydrostatic primitive equations.

Lastly, the density equation, Equation 2.17, can only be simplified by its diffusion term. The horizontal diffusion drops out and the resulting equation is Equation ??.

To summarize, the Boussinesq approximation and scale analysis results in the following hydrostatic primitive equations,

$$\frac{\partial \mathbf{u}_h}{\partial t} + \mathbf{u} \cdot \nabla \mathbf{u}_h + f \hat{\mathbf{k}} \times \mathbf{u}_h = -\frac{1}{\rho_0} \nabla_h p + \nu \nabla^2 \mathbf{u}_h \quad (2.18)$$

$$0 = -\frac{\partial p}{\partial z} - \rho g \quad (2.19)$$

$$\frac{\partial w}{\partial z} = -\nabla_h \mathbf{u}_h = 0 \quad (2.20)$$

$$\frac{D\rho}{Dt} = \kappa \frac{\partial^2 \rho}{\partial z^2} \quad (2.21)$$

where \mathbf{u}_h is the horizontal velocity components u and v .

2.2.3 Shallow Water Model

The shallow water model is a simplified model of the ocean commonly used to look at large scale ocean circulation patterns. There are numerous applications where the horizontal length scale is much larger than the vertical length scale and thus, these equations are quite useful. They have been used for solving various oceanic [65, 16], atmospheric problems as well as dam breaking [72, 79] and river flow problems [15].

The shallow water model can be derived from the hydrostatic primitive equations (Equations 2.18 - 2.21). Assuming that the flow is homogeneous (no stratification) and frictionless, the equations become,

$$\frac{\partial \mathbf{u}_h}{\partial t} + \mathbf{u} \cdot \nabla \mathbf{u}_h + f \hat{\mathbf{k}} \times \mathbf{u}_h = -\frac{1}{\rho_0} \nabla_h p \quad (2.22)$$

$$0 = -\frac{\partial p}{\partial z} \quad (2.23)$$

$$\nabla \cdot \mathbf{u} = 0 \quad (2.24)$$

Assuming that the horizontal flow field is initially independent of depth, then it will remain independent of depth at future times. Also, the pressure is independent of z because of Equation 2.23. Since all the advection terms, the Coriolis terms and the pressure terms are all independent of z , that means u and v will remain z -independent at all times. In geophysical fluid dynamics, flows under this assumption are called barotropic. Thus, the x and y momentum equations reduce to,

$$\frac{\partial \mathbf{u}_h}{\partial t} + \mathbf{u}_h \cdot \nabla \mathbf{u}_h + f \hat{\mathbf{k}} \times \mathbf{u}_h = -\frac{1}{\rho_0} \nabla_h p \quad (2.25)$$

where the subscript h can be dropped. Now, since the velocities are homogeneous in the z direction (or depth averaged), the same needs to be done to the continuity equation, Equation 2.24. The first two terms are independent of z , but a vertical velocity varying with depth can exist. Integrate Equation 2.24 over the entire fluid depth will give,

$$\left(\frac{\partial u}{\partial x} + \frac{\partial v}{\partial y} \right) \int_b^{b+\eta} dz + [w]_b^{b+\eta} = 0 \quad (2.26)$$

where b is a function describing the spatially varying bottom bathymetry and η is the sea surface height. For boundary conditions, the vertical velocity has to obey the following properties at the surface and bottom boundaries (particles on surface cannot leave surface, particles on the bottom cannot leave bottom),

$$w(z = b + \eta) = \frac{\partial(b + \eta)}{\partial t} + u \frac{\partial(b + \eta)}{\partial x} + v \frac{\partial(b + \eta)}{\partial y}$$

$$w(z = b) = \frac{\partial b}{\partial t} + u \frac{\partial b}{\partial x} + v \frac{\partial b}{\partial y}$$

therefore, Equation 2.26 becomes,

$$\frac{\partial \eta}{\partial t} + \frac{\partial(\eta u)}{\partial x} + \frac{\partial(\eta v)}{\partial y} = 0$$

This replaces the continuity equation and eliminates vertical velocity from the formulation. Dynamic pressure can also be calculated, it is homogeneous and independent of depth (assuming uniform atmospheric pressure over the ocean). This is,

$$p = \rho_0 g(\eta + b)$$

This pressure can be substituted into the momentum equations (Equation 2.25) and closes the problem with three equations and three unknowns. For a flat bottom ($b(x, y)$ does not vary spatially), the shallow water equations are

$$\frac{\partial u}{\partial t} + u \frac{\partial u}{\partial x} + v \frac{\partial u}{\partial y} - fv = -\frac{1}{\rho_0} \frac{\partial \eta}{\partial x} \quad (2.27)$$

$$\frac{\partial v}{\partial t} + u \frac{\partial v}{\partial x} + v \frac{\partial v}{\partial y} + fu = -\frac{1}{\rho_0} \frac{\partial \eta}{\partial y} \quad (2.28)$$

$$\frac{\partial \eta}{\partial t} + \frac{\partial(\eta u)}{\partial x} + \frac{\partial(\eta v)}{\partial y} \quad (2.29)$$

In this work, all three sets of equations have been investigated to see which worked best with the wavelet method and Brinkman penalization. In the following chapters, the use equations will be further described and results will be discussed. In the following section, an overview of how current ocean models solve these governing equations.

2.3 Ocean Circulation Modeling

There is an exhaustive list of ocean models used in scientific research [2]. Many of the large OGCMs, such as the ones used for climate prediction, have fixed spatial resolution [40, 30, 37, 68, 34, 35, 73]. However, there has been some initial progress made on the use of non-uniform grids, as well as adaptive grids. There are also various techniques that have been developed to handle the complex geometry that is inherent in ocean boundaries and bathymetry. These models and techniques will be reviewed below.

The current standard in the majority of ocean models is to use structured meshes [22], typically used with a finite difference method. A structured mesh is one that has a uniform topological structure, which means if one is given a node, they can determine implicitly what other nodes are connected to it. Thus, the topology of the mesh is uniform in space. Therefore, these meshes have a block structure, so that different structured meshes can be used and combined along the interface. This allows for higher resolution in certain regions of interest. This is known as a nested grid, which assumes that one knows a priori the location that refinement is needed as well as how much extra resolution is necessary. Some examples of this include Regional Ocean Modeling System (ROMS) [6], which is a free-surface, terrain-following, hydrostatic primitive equation ocean model. There is also [52, 45].

Vertical grids also traditionally use a structured mesh but there are three main choices for the vertical coordinate, as shown in Figure 2.7. The simplest and oldest is the z-coordinate model, which is when the vertical grid is aligned with surfaces of constant depth. The issue with using the z-coordinate is the difficulty in representing complex bathymetry without introducing sharp corners due to stair-step representation. A popular alternative is to employ partial cell or shaved cell, as shown in Figure 2.8. These techniques were used successfully by [5].

The other vertical coordinates include the σ -coordinate and isopycnal-coordinate models. The σ -coordinate conforms to both the bathymetry and the free surface. The isopycnal-coordinate model aligns with the surfaces of constant density. The biggest problem with the σ -coordinate is that there are substantial errors in the calculation of the horizontal pressure gradient [32]. The other big problem with the σ -coordinate model is that the number of vertical levels is held constant over the entire domain. More details can be found in [24].

There also exists a hybrid vertical coordinate model, which was developed to fix the issue with the constant vertical levels in the σ -coordinate model. This model uses the

σ -coordinates in the shallow regions, z-coordinates in the mixed layer and unstratified regions and isopycnal coordinates in the stratified regions [75, 29]. This model tries to take advantage of where each choice of vertical coordinate naturally behaves best.

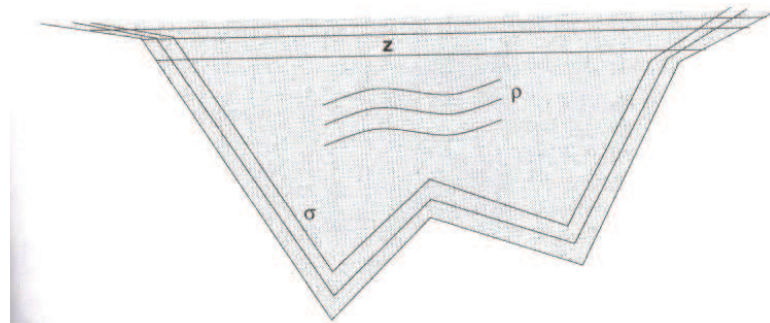


Figure 2.7: Illustration of three choices for a vertical coordinate.[38]

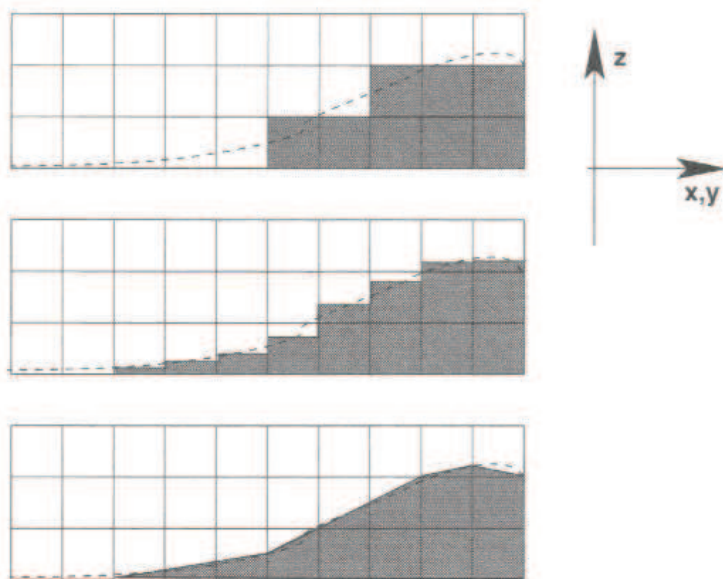


Figure 2.8: Three different representations of bottom topography with the z-coordinate. The top is called "full cell" and is the oldest, the middle is called "partial cell" and the bottom is called "shaved cell".[38]

On the other hand, unstructured meshes are less mainstream for ocean models but becoming more popular. Unstructured meshes allow for an arbitrary mesh structure and are typically solved using finite element, finite volume, and/or spectral methods. This flexibility allows for a better representation of the coastline and bathymetry. The use of unstructured meshes is especially prevalent in fields of engineering that work with exterior or interior pipe flow, aircraft wings, etc (some examples include [14, 39, 63]).

The recent review article, [57], gives a extensive overview of what is being done with unstructured adaptive meshes in ocean modeling. In summary, models with unstructured meshes have been relatively underused over the models with structured meshes in the ocean community. What follows is a short description of the most well known ocean models using unstructured grids.

The SUNTANS model from Stanford [62] is also a well-known unstructured-grid model. In this model, the non-hydrostatic primitive equations are solved using a finite-volume method. They also use an immersed boundary method to represent the bathymetry. This is one of the few models that includes the non-hydrostatic dynamics.

There is also the SEOM [51], which is a three-dimensional hydrostatic spectral element model with sigma coordinates in the vertical. The same group has also done some work with the shallow water equations [16].

The ICOM model from Imperial College which is a non-hydrostatic finite-element model [12, 71, 31, 50]. In this model, they use parallel load-balanced anisotropic adaptive meshes in 3D, so there is no difference in the horizontal and vertical meshes.

MIT also has a finite-volume, non-hydrostatic ocean model called MITgcm [54]. They did several studies that compared hydrostatic, quasi-hydrostatic and non-hydrostatic, [55]. They found that the non-hydrostatic models were just as computational efficient as the hydrostatic models when run in the hydrostatic limit [56].

Other unstructured models include the QUODDY finite element 3D hydrostatic model [25], the FEOM finite element 3D hydrostatic model [74], the SLIM finite element

3D hydrostatic model [90], and FVCOM a finite volume 3D hydrostatic model [13]. They all do something a little different with the horizontal meshes and with what combination of vertical coordinate and mesh they use.

Finally, there is an additional topic of mesh adaptivity. It is clear that having a non-uniform or unstructured mesh is ideal for the majority of ocean simulations. However, due to the large range of spatial and temporal scales, which are also coupled, the need for a model that can also dynamical adapt on the solution is also beneficial and even necessary for accuracy. Many processes in ocean modeling are parameterized, but there are many that could easily resolved by having a model that is able to on-the-fly vary its resolution. [57]

There are a few models being used that use mesh adaptivity. These include both unstructured and structured grids. The ICOM model is the best example of one using an unstructured grid [50, 49, 12]. Another unstructured mesh optimization algorithm is used by [65] uses the shallow water model.

For structured mesh models, the most common technique is adaptive mesh refinement (AMR). AMR is similar to the nested grid technique, but much more powerful since there can be many levels of refinement and they can evolve dynamically based on the structure of the solution. The problem with AMR methods is there are numerical issues with the discrete jumps in resolution. Some finite difference models that use AMR include [28] and [44]. There is also a finite volume ocean model which uses quadtree refinement, a form of AMR, in the horizontal [76].

2.4 Adaptive Wavelet Collocation Method

The adaptive mesh numerical technique used is called adaptive wavelet collocation method (AWCM) and was developed by Vasilyev and and collaborators [84, 86]. It is a general method that uses second generation wavelets to efficiently solve partial differential equations. In this section, we will briefly review this methodology.

The benefit of using wavelets is that they are localized in both space and time. They are ideal for use in complex flows where localized structures exist in the solution. The wavelet collocation method takes advantage of wavelet compression properties. Functions with localized structures or regions with sharp transitions are well compressed using wavelet decomposition. This compression is achieved by keeping only the wavelets with coefficients that are greater than an a priori given threshold parameter, thus how the grid adaptation works. This allows high resolution computations to be carried out only in the regions where it is necessary. It also allows a solution to be obtained on a near optimal grid for a given accuracy.

Any function $u(\mathbf{x})$ in an n -dimensional space can be decomposed as [17, 26, 53]

$$u(\mathbf{x}) = \sum_{\mathbf{k} \in \mathcal{K}^0} c_{\mathbf{k}}^0 \phi_{\mathbf{k}}^0(\mathbf{x}) + \sum_{j=0}^{+\infty} \sum_{\mu=1}^{2^n-1} \sum_{\mathbf{l} \in \mathcal{L}^{\mu,j}} d_{\mathbf{l}}^{\mu,j} \psi_{\mathbf{l}}^{\mu,j}(\mathbf{x}) \quad (2.30)$$

where $\phi_{\mathbf{k}}^0(\mathbf{x})$ are scaling functions on the lowest level of resolution and $\psi_{\mathbf{l}}^{\mu,j}(\mathbf{x})$ are the wavelet basis functions. Also, $c_{\mathbf{k}}^0$ and $d_{\mathbf{l}}^{\mu,j}$ are the scaling and wavelet coefficients, respectively. These wavelet coefficients $d_{\mathbf{l}}^{\mu,j}$ will be small except near areas with large gradients. Equation 2.30 can be decomposed into two terms whose wavelet coefficients are above and below a chosen threshold parameter ϵ ,

$$u(\mathbf{x}) = u_{\geq}(\mathbf{x}) + u_{<}(\mathbf{x}), \quad (2.31)$$

where

$$u_{\geq}(\mathbf{x}) = \sum_{\mathbf{k} \in \mathcal{K}^0} c_{\mathbf{k}}^0 \phi_{\mathbf{k}}^0(\mathbf{x}) + \sum_{j=0}^{+\infty} \sum_{\mu=1}^{2^n-1} \sum_{\substack{\mathbf{l} \in \mathcal{L}^{\mu,j} \\ |d_{\mathbf{l}}^{\mu,j}| \geq \epsilon \|u\|}} d_{\mathbf{l}}^{\mu,j} \psi_{\mathbf{l}}^{\mu,j}(\mathbf{x}), \quad (2.32)$$

$$u_{<}(\mathbf{x}) = \sum_{j=0}^{+\infty} \sum_{\mu=1}^{2^n-1} \sum_{\substack{\mathbf{l} \in \mathcal{L}^{\mu,j} \\ |d_{\mathbf{l}}^{\mu,j}| < \epsilon \|u\|}} d_{\mathbf{l}}^{\mu,j} \psi_{\mathbf{l}}^{\mu,j}(\mathbf{x}), \quad (2.33)$$

Donoho [27] was able to show that for a regular function the error is bounded as

$$\|u(\mathbf{x}) - u_{\geq}(\mathbf{x})\| \leq C_1 \epsilon \|u\|, \quad (2.34)$$

which means that the number of grid points needed to solve a numerical problem can be significantly reduced while still retaining a prescribed level of accuracy determined by the threshold parameter ϵ .

In the wavelet collocation method there is a one-to-one correspondence between grid points and wavelets. Thus, this makes calculation of nonlinear terms simple, and allows the grid to adapt automatically to the solution at each time step by adding or removing wavelets. In addition to the points with high enough wavelet coefficients, there are several other checks done to make sure the resolution is sufficient for the given simulation. The way the methods works is, at the beginning of each time step, the wavelet coefficients are calculated. All the wavelets with coefficient magnitudes less than an threshold ϵ are removed. The points kept are called significant points. It can be shown that the L_∞ error for this approximation is bounded by ϵ . Next, to account for the evolution of the solution over time, the nearest neighbor wavelet coefficients in position and scales are added [48], which is the adjacent zone. This allows the grid to automatically follow the evolution of the solution. Then, reconstructions points are added, which are points needed to compute the wavelet transforms. Lastly, ghost points are added, these are points needed to calculate spatial derivatives. The spatial derivatives are calculated using finite differences. Since this method uses second generation wavelets [80], the order of the wavelet (and also finite difference) can be easily varied.

Figure 2.9 shows a one-dimensional example of a solution and its grid. It also shows the grid at various levels of resolution (the y-axis). It is clear the the location in the center of the x-axis where the solution has a sharp gradient has localized refinement and needs points at higher levels of resolution.

There are some additional computational costs associated with the use of the

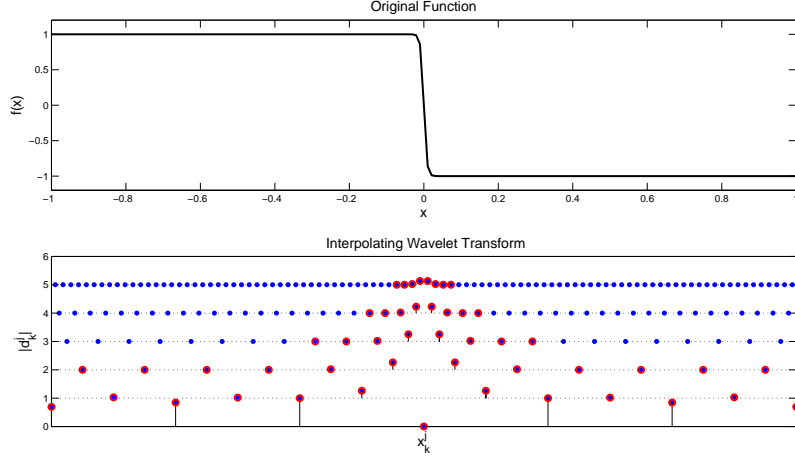


Figure 2.9: A one dimensional example of grid adaptation using the Adaptive Wavelet Collocation method.

adaptive multi-resolution wavelet method. Currently, the cost per grid point is approximately three to five times greater than the cost of a standard non-adaptive method. However, in cases of large compressions [61] (up to 10^3), the compression greatly outweighs this cost. There is also some memory savings associated with using adaptive methods, which allows higher resolution simulations to be run with the same computational resources.

In summary, the dynamically adaptive wavelet collocation method is an adaptive, variable order method for solving partial differential equations with localized structures that change their location and scale in space and time. Because the computational grid automatically adapts to the solution (in position and scale), we do not have to know *a priori* where the regions of high gradients or structures exist. In related work the dynamically adaptive wavelet collocation method has been combined with the Brinkman penalization method [42, 41] to define solid structures in the domain for the simulation of complex geometry flows.

2.5 Brinkman Penalization

2.5.1 Methods for Representing Boundaries with Complex Geometries

In ocean modeling, one of challenges in how to accurately represent the coastal boundaries and the bathymetry of the ocean floor. With the inherent complicated geometry that exists, there are two general techniques used mostly commonly. The first is body-fitted grids, which have been used by fluid dynamics community for some time [81, 58]. As mentioned in Section 2.3, the majority of ocean models are using structured or unstructured body-fitted grid methods. These methods generate grids to conform to the complex boundaries, which can be very expensive. This makes for easy implementation of boundary conditions, but in order to resolve boundary layers there is a need for a fine resolution near the boundary. Since most ocean models do not have adaptive or even non-uniform grids, this can be too expensive. Even for the structured and unstructured meshes that are adaptive and non-uniform, the grid generation and solution interpolation to the new mesh is prohibitively expensive.

The other approach for representing complex geometries is immersed boundary methods [67, 60]. These methods work by carrying out simulations on non-body conformal fixed Cartesian grids and then formulated a procedure that imposes immersed boundary effects on the fluid. It makes for straightforward implementation of solid boundaries of arbitrary complexity.

2.5.2 Immersed Boundary Methods for Incompressible Flows

Immersed boundary methods were originally introduced by Peskins for biomedical applications of flow patterns around heart valves, for incompressible viscous flows [66]. In this case, the immersed boundary is modeled as elastic media, which exerts localized forces on the fluids through a modification of the momentum equations. This was also done for a solid obstacle, where a stiff spring with a restoring force was used instead

of the elastic media [46]. This method was then extended, to use a feedback forcing to represent the immersed boundary effects for rigid body problems [36, 77]. The problem with these immersed boundary methods is that they all use an explicit time step. For these stiff problems, the result is a very restrictive time step. Additionally, they all use non-adaptive grids, which are very inefficient for high Reynolds number boundary layer flows. Lastly, there is no mathematical convergence proof for any of these methods.

There are a few other immersed boundary techniques for incompressible viscous flow that use external forces to simulate the immersed boundary. There is Cartesian grid methods [69, 21, 92, 10] and ghost-cell methods [82], which directly impose the boundary conditions on the immersed boundary.

The SUNTANS model from Standford [62] is using immersed boundary methods.

2.5.3 Brinkman Penalization for Incompressible Flows

Another immersed boundary method is the Brinkman penalization method, originally proposed by Arquis and Caltagirone [9]. It is a volume penalization technique where the boundary conditions are imposed by adding the penalization terms to the momentum equations, similar to the Peskin's immersed boundary methods. Brinkman penalization works by modeling solid obstacles and boundaries as porous media and setting the parameters associated with the porous media in the limit of a solid body. There are many benefits to using Brinkman penalization over the other immersed boundary methods. The first is that it can be used with any numerical method or grid. Since it only directly modifies the equations, how you solve the equations does not change the method. Its main advantage is that the error can be estimated rigorously in terms of the penalization parameter [64]. Lastly, it can be shown that the solutions of the penalized incompressible Navier-Stokes equations strongly converges to the exactly solution as the penalization parameter approaches zero [8].

This formulation of Brinkman penalization can be used for the primitive equa-

tions, since it is in the same form as the incompressible Navier-Stokes equations. Figure 2.10 shows a schematic of traditional boundary conditions versus Brinkman penalization.

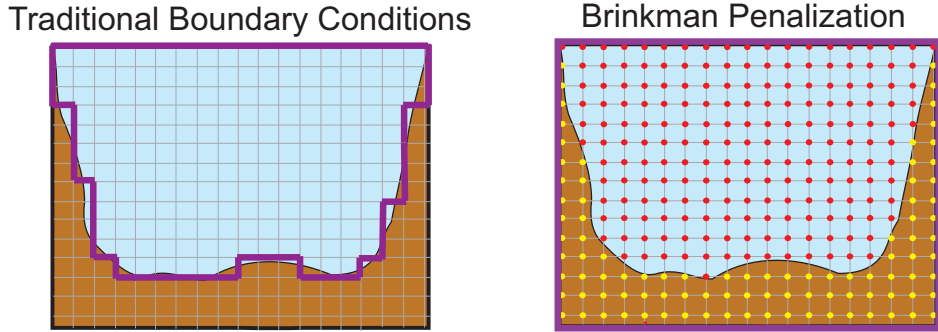


Figure 2.10: A schematic of traditional boundary conditions versus brinkman penalization.

2.5.4 Immersed Boundary Methods for Compressible Flows

Immersed boundary methods are less popular for compressible viscous flows. There were some developments with the Cartesian grid method to simulate compressible flows around a circular cylinder and an airfoil at high Reynolds numbers. In this case, the acoustic wave reflection and transmission at the interface between the fluid and solid was not taken into account, which is critical. Another technique is the Impedance Mismatch Method, which is used to model the acoustic wave propagation around solid wall boundaries using the non-body conformal cartesian grids. This method was originally developed by Chung [18] and later used for linearized acoustic problems with steady mean flows [19, 47, 7]. This method works by setting a larger characteristic impedance inside the solid obstacle or boundary so that most acoustic waves are reflected by the classical theory of acoustics. The errors associated with this method are not sufficiently accurate in some cases. Another drawback is that this method has no one of imple-

menting no-slip boundary conditions or other immersed boundary conditions.

2.5.5 Brinkman Penalization for Compressible Flows

Brinkman penalization was extended to compressible flow by Liu and Vasilyev [70]. In addition to penalizing the momentum and energy equations as in done the incompressible formulation, the continuity equation for porous media is considered inside obstacles. Therefore, the penalized porous region acts as a high impedance medium and results in negligible wave transmissions. The results of the direct numerical simulations were in excellent agreement with the analytical solutions and the numerical simulations verify the accuracy and convergences rates.

The compressible formulation of Brinkman penalization can be extended to work for the shallow water equations. The shallow water equations are mathematically equivalent to the compressible gas dynamic equations, for which this formulation was developed. Further details about the extension are in the following chapters.

Chapter 3

Shallow Water Model

As a first step of investigating how ocean circulation models can be solved using the adaptive wavelet method, the shallow water model was studied. This 2D model is a simplified version of the full oceanic primitive equations.

3.1 Physical Model and Governing Equations

The shallow water model is derived from depth averaging the hydrostatic primitive equations under the assumption that the vertical length scale is much smaller than the horizontal length scale (details in Section 2.2). Therefore, there is no stratification.

$$\frac{\partial \eta}{\partial t} = -\nabla \cdot (\eta \mathbf{u}) \quad (3.1)$$

$$\frac{\partial \mathbf{u}}{\partial t} + \mathbf{u} \cdot \nabla \mathbf{u} + \frac{1}{Ro} f \hat{\mathbf{k}} \times \mathbf{u} = -\frac{1}{Fr^2} \nabla \eta$$

where η is the sea surface height, u and v are the horizontal components of velocity, f is the Coriolis force, Ro is the Rossby number and Fr is the Frouard number.

The free surface allows for propagation of gravity waves, which travel at $c = \sqrt{gH}$. These are equivalent to acoustic waves in the compressible gas dynamic equations.

3.2 Brinkman Penalization Method for Shallow Water Model

The shallow water equations are mathematically equivalent to the Euler equations. A compressible formulation of Brinkman penalization was developed by Liu and

Vasilyev [70]. This compressible form was extended to the shallow water equations,

$$\frac{\partial \eta}{\partial t} = -[1 + (\frac{1}{\phi} - 1)\chi] \nabla \cdot (\eta \mathbf{u}) \quad (3.2)$$

$$\frac{\partial \mathbf{u}}{\partial t} + \mathbf{u} \cdot \nabla \mathbf{u} + \frac{1}{Ro} f \hat{\mathbf{k}} \times \mathbf{u} = -\frac{1}{Fr^2} \nabla \eta - \frac{\chi}{\eta_{pen}} \mathbf{u}$$

where the Brinkman penalization parameter, $\eta_{pen} \ll 1$ and the porosity parameter, $\phi \ll 1$. And where,

$$\chi(\mathbf{x}, t) = \begin{cases} 1 & \text{if } \mathbf{x} \in O(\mathbf{x}), \\ 0 & \text{otherwise} \end{cases}$$

where $O(\mathbf{x})$ is some obstacle or in the case of oceans, land or the ocean floor.

Since the shallow water equations are mathematically similar to the compressible gas dynamic equations, the extension seemed straight-forward. However, after thorough analysis of the equations and numerical testing, it was found that there are three main differences between the shallow water equations and the gas dynamics equations. These differences results in a slightly different treatment of the penalization parameters and numerical set up.

The following analysis describes these differences, while also going through the amplitude and phase error analysis for the case of gravity wave propagation in the small amplitude limit.

3.2.1 Wave Speeds

One of the assumptions that is made when doing the error analysis for compressible Brinkman penalization was the speed of sound was the same in the fluid region and porous media region. It was found for the penalized shallow water equations, the gravity wave speed was different in the fluid versus the porous media. Let's consider the one dimensional shallow water equations,

$$\frac{\partial \mathbf{u}}{\partial t} + \mathbf{A} \frac{\partial \mathbf{u}}{\partial x} = 0 \quad (3.3)$$

where $\mathbf{u} = (\eta, \eta u)^T$ is the vector of conservative, dimensional variables and the Jacobian matrix is,

$$\mathbf{A} = \begin{bmatrix} 0 & \frac{1}{\phi} \\ g\eta - \frac{(\eta u)^2}{\eta^2} & \frac{2(\eta u)}{\eta} \end{bmatrix}$$

Note that when $\phi = 1$, the equations reduce to the traditional shallow water equations. Therefore, $\phi = 1$ represents the fluid case, while all other cases are for the porous media. To find the gravity wave speed in both regions, the eigenvalues of the Jacobian matrix, \mathbf{A} , can be found by solving,

$$|\mathbf{A} - \lambda \mathbf{I}| = 0$$

which gives,

$$\lambda^2 - 2u\lambda + \frac{1}{\phi}(u^2 - g\eta) = 0$$

solving for the roots,

$$\lambda = u \pm \sqrt{u^2 - \frac{1}{\phi}(u^2 - g\eta)} \quad (3.4)$$

With some scale analysis, Equation 3.4 can be simplified. Assuming that $u \ll \phi$ and $\eta = H + \epsilon$, where H is the mean depth of the ocean and ϵ is some small perturbation ($\epsilon \ll H$). Thus, the eigenvalues become,

$$\lambda = u^2 \pm \sqrt{\frac{gH}{\phi}} \quad (3.5)$$

When $\phi = 1$, the eigenvalues are $u \pm \sqrt{gH}$, as expected for shallow water gravity wave speed. However, for the any other ϕ value, the eigenvalues are not the same. Since $\phi \ll 1$ for the Brinkman penalization formulation, the gravity wave speed inside the porous media is much larger than that in the fluid region.

3.2.2 Impedance

This section looks at some properties associated with the classical theory of acoustics [11] that were used in the development of the compressible formulation of Brinkman

penalization [70]. Thus, consider the plane wave reflection and transmission at the interface between two different media. To model the one dimensional problem of wave propagation in a fluid to porous media, it can be thought of as a sudden change in cross-sectional area. From the acoustics theory, the acoustic impedance at a given surface is the ratio of the surface-averaged acoustic pressure to the fluid volume velocity,

$$Z = \frac{\rho c}{S}$$

where ρ is density, c is gravity wave speed in the fluid ($c = \sqrt{gH}$), and S is the cross-sectional area. In order to have most of the wave reflected, the obstacle's acoustic impedance needs to be sufficiently large, the basis for Impedance Mismatch Method [18]. For the case of the shallow water equations, since the gravity wave speed is also a function of ϕ , the impedance becomes,

$$Z = \frac{\rho c}{\phi^{3/2}}$$

which is a higher impedance than what was found for the compressible Brinkman penalization formulation, which was $Z = \frac{\rho c}{\phi}$. This allows for a slightly lower range of reasonable ϕ values allowed for negligible wave transmission in the shallow water case over the compressible gas case. This is a nice feature of this extension of Brinkman penalization.

3.2.3 Amplitude and Phase Errors by Asymptotic Analysis

The use of asymptotic analysis will provide a way to estimate the amplitude and phase errors associated with the penalized shallow water equations. In addition, by looking at the equations in different asymptotic limits, it provides information about the behavior of the system from a rigorous mathematical viewpoint. The following analysis is assumed small amplitude waves in the ocean region and was derived from work done on the penalized compressible gas dynamic equations [70].

3.2.3.1 Asymptotic Analysis for Ocean Region

For the ocean region, the variables can be written as,

$$\eta_o = 1 + \epsilon \eta'_o \quad (3.6)$$

$$u_o = \epsilon u'_o \quad (3.7)$$

where $\epsilon \ll 1$. If Equations 3.6 and 3.7 are substituted into Equations 3.2 and 3.2 and only the leading perturbation terms are kept, the result is a wave equation,

$$\frac{\partial^2 \eta'_o}{\partial t^2} = \frac{\partial^2 \eta'_o}{\partial x^2} \quad (3.8)$$

$$\frac{\partial^2 u'_o}{\partial t^2} = \frac{\partial^2 u'_o}{\partial x^2} \quad (3.9)$$

3.2.3.2 Asymptotic Analysis for Continental Region

For the continental region, the variables can be written as,

$$\eta_c = 1 + \epsilon \eta'_c \quad (3.10)$$

$$u_c = \epsilon \eta_{pen} u'_c \quad (3.11)$$

The leading perturbation terms in this case are different from the ocean region because of the strong Brinkman damping term in the momentum equation. If Equations 3.10 and 3.11 are substituted into Equations 3.2 and 3.2 and only the leading order terms are kept, the result is a diffusion equation,

$$\frac{\partial \eta'_c}{\partial t} = \alpha \frac{\partial^2 \eta'_c}{\partial x^2} \quad (3.12)$$

$$\frac{\partial u'_c}{\partial t} = \alpha \frac{\partial^2 u'_c}{\partial x^2} \quad (3.13)$$

where $\alpha = \frac{\eta_{pen}}{\phi}$.

3.2.3.3 Asymptotic Analysis for Boundary Layer

The asymptotic analysis for the ocean and continental region is only valid away from the interface, because of the length and magnitude scales of the perturbations used. For the boundary layer, the variables can be written as,

$$\eta_{\text{bl}} = 1 + \epsilon \eta'_{\text{bl}} \quad (3.14)$$

$$u_{\text{bl}} = \epsilon \eta_{\text{pen}} u'_{\text{bl}} \quad (3.15)$$

If Equations 3.14 and 3.15 are substituted into Equations 3.2 and 3.2 and only the leading order terms are kept, the result is a diffusion equation,

$$\frac{\partial \eta'_{\text{bl}}}{\partial t} = \alpha \frac{\partial^2 \eta'_{\text{bl}}}{\partial x^2} \quad (3.16)$$

$$\frac{\partial u'_{\text{bl}}}{\partial t} = \alpha \frac{\partial^2 u'_{\text{bl}}}{\partial x^2} \quad (3.17)$$

This is where the penalized shallow water equations differ greatly from the penalized compressible gas dynamic equations. For the compressible gas dynamic equations, it was found that there was a boundary layer region that transitioned the two other asymptotic solutions nicely [70]. Therefore, in addition to the fluid region being governed by the acoustic wave equation and the porous media region being governed by a diffusion equations, there exists a boundary layer region in between that is governed by a diffusive wave equation. This boundary layer does not exist in the penalized shallow water equations. It has been shown here, that the boundary layer is the same as the continental region, leaving no natural, mathematical transition. As a result, numerical techniques need to be employed to create that transition to maintain numerical stability.

Additionally, it was found for the compressible gas dynamic formulation that it wasn't necessary to resolve the boundary layer. For the shallow water formulation,

it is necessary to resolve the numerical boundary layer. This makes it slightly more expensive. However, since the shore of the ocean is not necessarily a solid wall, it seems that modeling it as a slightly gradual change from fluid to solid may result in a more accurate representation. It does not seem necessary to have a sharp transition. As a result, the computational cost can be minimized. Either way, the theory works in the limit of a solid wall given the proper computational resources.

3.3 Benchmark Problem I: One Dimensional normal wave

To verify convergence of the method, a one dimensional test case was used. A one dimensional normal wave was initialized for the sea surface height. The velocity was initialized to zero, as shown in Figure 3.1.

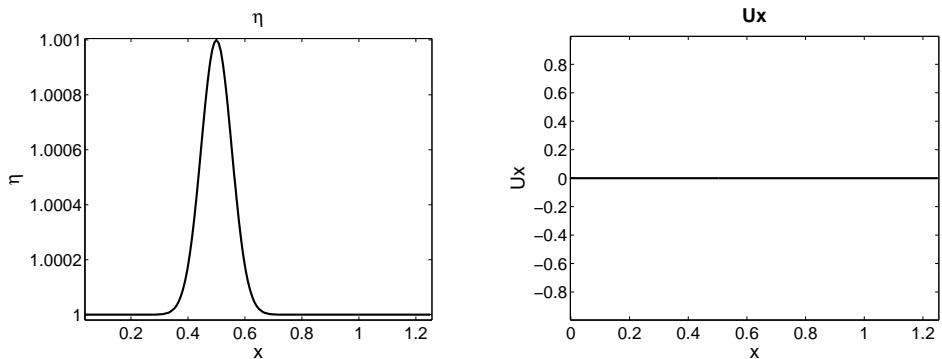


Figure 3.1: Initial conditions for 1D wave.

The wave splits and propagates to the east and west. On the east side, it hits a Brinkman zone and on the west side, it hits a regular no slip boundary wall. This allowed for comparison between the two methods. After complete reflection, the solution is shown in Figure 3.2.

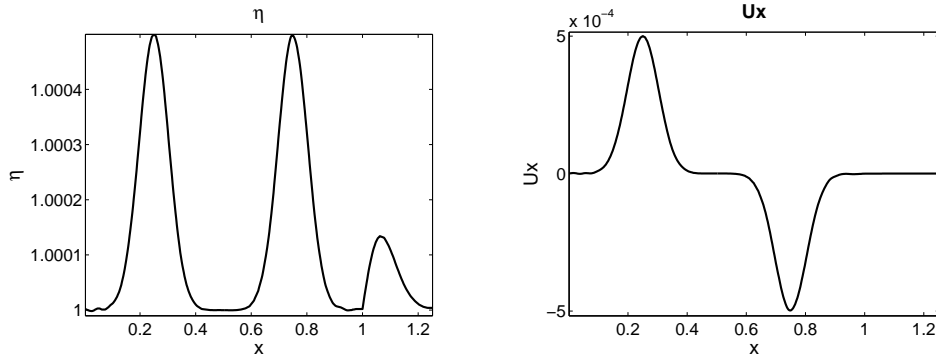


Figure 3.2: 1D wave after complete reflection.

Figure 3.2 not only demonstrates how the no slip boundary conditions are satisfied on the Brinkman wall, but also shows the decaying solution for sea surface height in the Brinkman zone. The small decay solution is negligible because it is actually multiplied by ϕ .

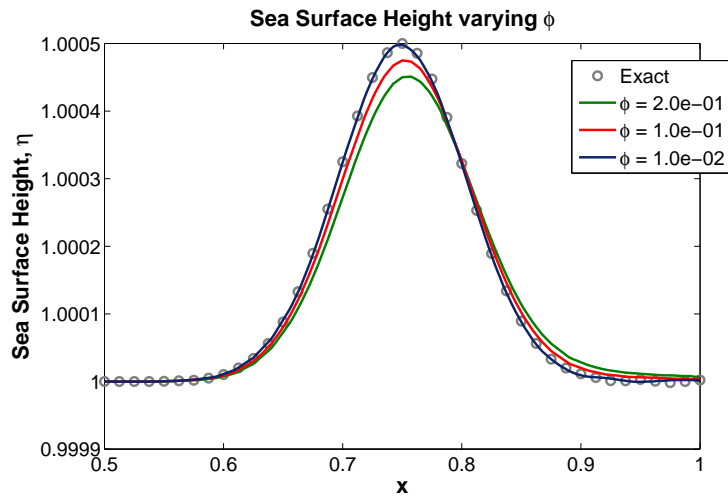


Figure 3.3: Plot of sea surface height for various porosity parameters.

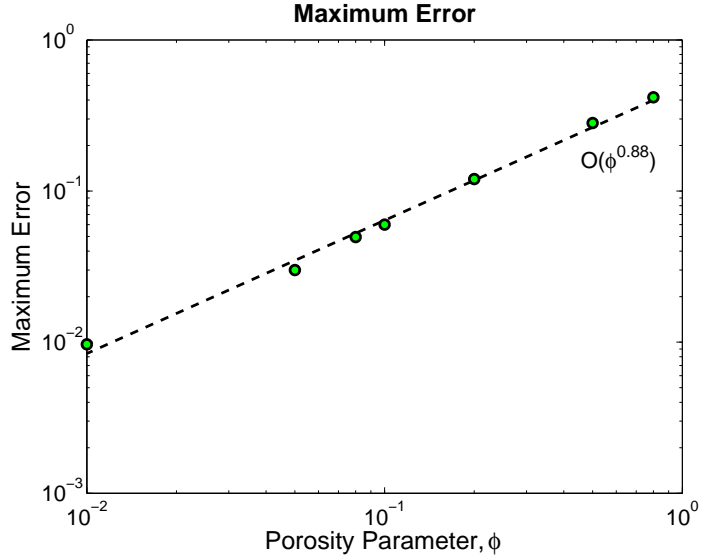


Figure 3.4: Plot of max error versus porosity parameter, ϕ , which demonstrates convergence of $O(0.88)$

3.4 Two-dimensional Wind-driven Double Gyre with Brinkman

Various 2D studies have been done to verify the new formulation of Brinkman penalization. First, a 2D wind-driven double gyre test case was run on a rectangular domain. This was done with traditional no-slip boundary conditions in one case and with Brinkman penalization (and straight boundaries) in another case. These two cases compare nicely visually, as can be seen in Figure 3.5. Further work needs to be done to more thoroughly analyze these 2D results.

Initial studies of variable topography have also been done. This cannot be compared to traditional boundary conditions, but can verify the stability of the method. There is a short transient time for this steady state solution to adjust to the Brinkman penalization. This is the case for a rectangular domain, as well. It takes the solution a slightly longer to adjust for a non-rectangular domain. However, if one could start with better initial conditions, then this can be avoided. Since, we are interested in a steady

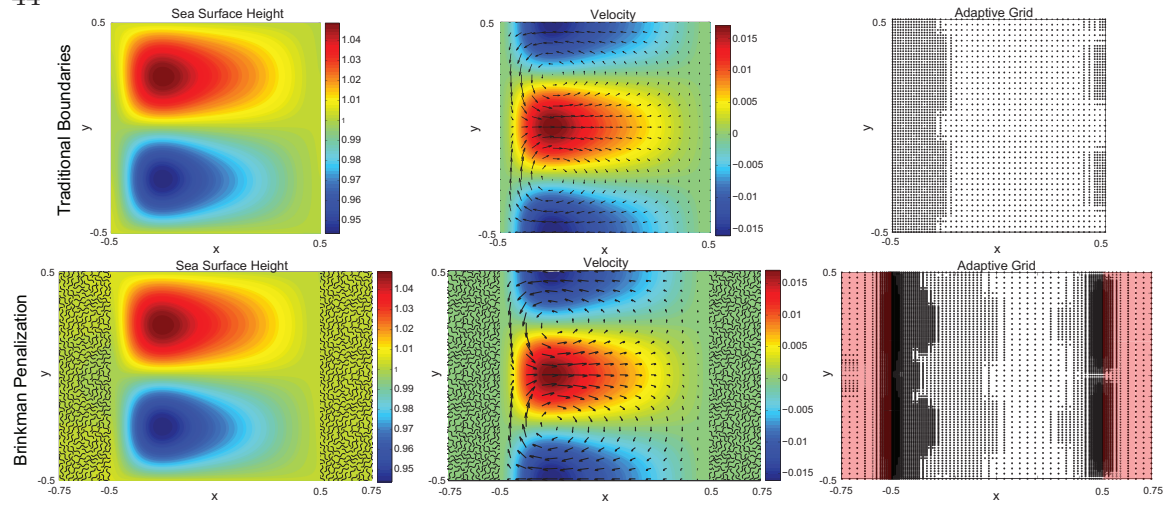


Figure 3.5: 2D plots of sea surface height, velocity, and the adaptive grid for a wind-driven double gyre circulation using Brinkman penalization.

state solution, this is not an issue.

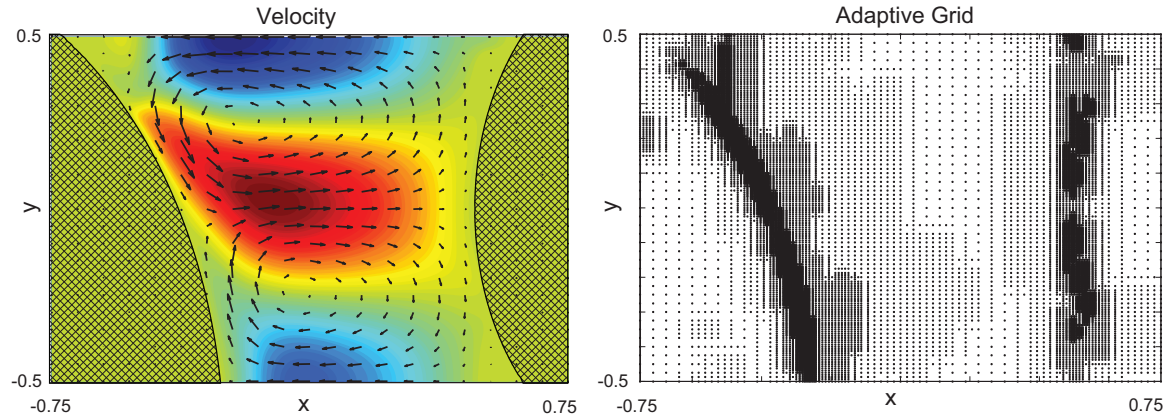


Figure 3.6: 2D plots of velocity and the adaptive grid for a wind-driven double gyre circulation using Brinkman penalization for variable topography.

Chapter 4

Hydrostatic Primitive Equations

To begin working on 3D simulations of the ocean, we began with the most commonly used set of governing equations: the hydrostatic primitive equations [59].

4.1 Physical Model and Governing Equations

The hydrostatic primitive equations are the Navier-Stokes equations with under the effect of rotation and assuming hydrostatic pressure (details in Section 2.2). In addition, there is conservation of mass (incompressible) and an open lid condition governed by a kinematic boundary condition.

$$\frac{\partial \eta}{\partial t} + (\mathbf{u}_h|_{z=z_{max}}) \cdot \nabla_h \eta = (w|_{z=z_{max}})$$

$$\frac{\partial \mathbf{u}_h}{\partial t} + \mathbf{u} \cdot \nabla \mathbf{u}_h + \frac{1}{Ro} f \hat{\mathbf{k}} \times \mathbf{u}_h = -\nabla_h P + \frac{1}{Re} \nabla^2 \mathbf{u}_h$$

$$\frac{\partial w}{\partial z} = -\nabla_h \mathbf{u}_h, (w|_{z=z_{bottom}(\mathbf{x}_h)}) = 0$$

$$\frac{\partial P}{\partial z} = -\frac{1}{Fr^2}, P|_{z=z_{max}} = \frac{\eta}{Fr^2}$$

Currently, a constant eddy viscosity model is being used for turbulence modeling. Also, for development purposes, there is no stratification and no tracking of the scalar transport variables. After all the features and numerics are fully implemented and tested,

more sophisticated turbulence modeling and variable density capabilities will be added.

Additionally, the Coriolis effect is not incorporated in any of the 2D results.

To start, an analytic linearized solution was used for initialization (no forcing and periodic boundaries). The numerical results converged to the analytic linearized solution within the numerical accuracy of the method. This case has been used for testing convergence of any numerical techniques added or developed specifically for ocean modeling capabilities.

For most of the work presented here, the test case used is a 2D wind-driven model that is initially at rest. The wind is incorporated through the forcing term in the momentum equation, \vec{F}_{wind} . An analytic function that varies sinusoidally in one horizontal direction and as a gaussian in the vertical direction is used to model the effects of the wind.

4.2 Extension of Brinkman Penalization

The ocean bathymetry is a hugely varying, intricate, and complex surface. Using current techniques for representation of this bottom boundary results in a surface that is either too crude (stair step representation) or too expensive (body-fitted meshes). The Brinkman penalization approach combined with an adaptive grid, can make the implementation of complex geometry boundaries accurate and feasible for even a simulation run on a standard desktop computer.

Brinkman penalization works by penalizing the equations in such a way that the boundary conditions are automatically satisfied. This is done by solving the regular governing equations in the fluid region, which is determined by some mask function. The rest of the computational domain is marked as the solid region and in this region the penalized form of the equations are solved. Figure 4.1 shows a comparison of the stair-step representation of boundary conditions, the Brinkman penalization method and our current implementation (which separates the continental topology and bottom

bathymetry).

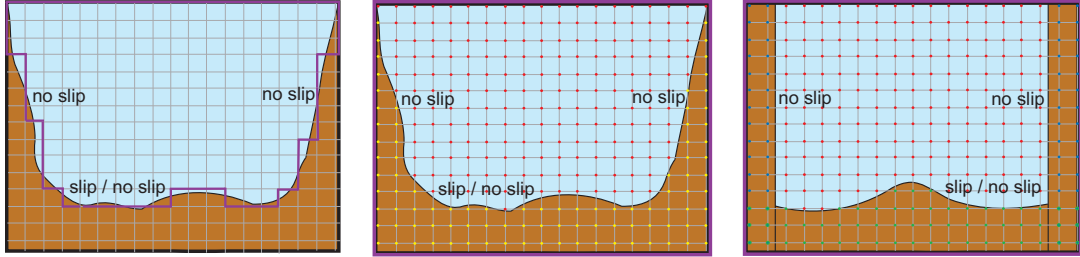


Figure 4.1: Outlined in purple is computational domain. Fluid domain is blue and solid domain is brown. Left: The current stair-step representation of boundary conditions in most ocean models. Middle: Brinkman Penalization Right: The current implementation with separation of the continental topology and bottom bathymetry.

The incompressible formulation of Brinkman penalization [9] is implemented by adding the term, $-\frac{\chi}{\eta_{pen}} \mathbf{u}$, to the momentum equations. This term forces the velocity to zero in the Brinkman zone. As a first attempt to utilize volume penalization to represent ocean boundaries, Brinkman penalization for no slip boundary conditions was used as a benchmark case. Results are shown in Figure 4.2 compared against no slip conditions directly applied to the boundaries.

Also, the convergence of the no slip Brinkman penalization was verified. Figure 4.3 shows the error convergence with decreasing the penalization parameter.

Comparison of the solution profiles demonstrates accurate representation of no slip conditions using this method. However, for the large scale ocean modeling of interest, no slip boundary conditions are not necessary or realistic. To avoid resolving the boundary layer associated with no slip conditions, it was necessary to extend this

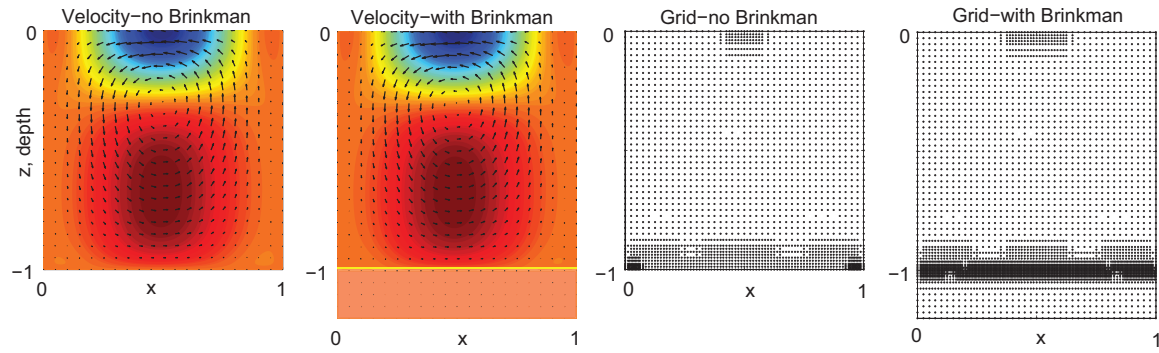


Figure 4.2: Demonstration of no slip boundary conditions with and without Brinkman penalization.

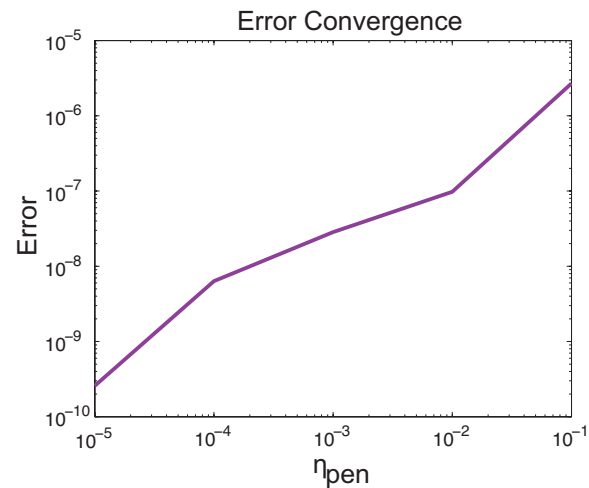


Figure 4.3: A plot of error convergence for decreasing penalization parameter for no slip conditions..

methodology to slip conditions, $\frac{\partial u}{\partial z} = \kappa u$. The idea is very similar to the no slip case, although, some numerical complications arose that made its implementation slightly more complicated. Figure 4.4 shows a schematic of the equations to be solved in each region for slip conditions to be satisfied.

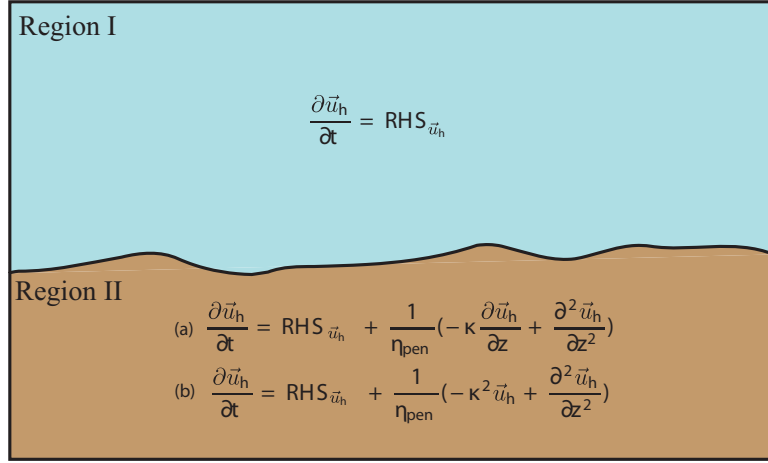


Figure 4.4: Diagram of how Brinkman penalization can be extended to slip conditions with the equations needed to be solved in each region.

Two different volume penalization methods were developed and tested. The full set of penalized governing equations are,

$$\frac{\partial \eta}{\partial t} + (\mathbf{u}_h|_{z=z_{max}}) \cdot \nabla_h \eta = (w|_{z=z_{max}})$$

(a)

$$\frac{\partial \mathbf{u}_h}{\partial t} + \mathbf{u} \cdot \nabla \mathbf{u}_h + \frac{1}{Ro} f \hat{\mathbf{k}} \times \mathbf{u}_h = -\nabla_h P + \frac{1}{Re} \nabla^2 \mathbf{u}_h + \frac{\chi}{\eta_{pen}} \left(-\kappa \frac{\partial \mathbf{u}_h}{\partial z} + \frac{\partial^2 \mathbf{u}_h}{\partial z^2} \right)$$

(b)

$$\frac{\partial \mathbf{u}_h}{\partial t} + \mathbf{u} \cdot \nabla \mathbf{u}_h + \frac{1}{Ro} f \hat{\mathbf{k}} \times \mathbf{u}_h = -\nabla_h P + \frac{1}{Re} \nabla^2 \mathbf{u}_h + \frac{\chi}{\eta_{pen}} \left(-\kappa^2 \mathbf{u}_h + \frac{\partial^2 \mathbf{u}_h}{\partial z^2} \right)$$

$$\frac{\partial w}{\partial z} = -\nabla_h \mathbf{u}_h, (w|_{z=z_{bottom}(\mathbf{x}_h)}) = 0$$

$$\frac{\partial P}{\partial z} = -\frac{1}{Fr^2}, P|_{z=z_{max}} = \frac{\eta}{Fr^2}$$

where,

$$\chi = \begin{cases} 1 & \text{if } x \in O_i \\ 0 & \text{otherwise} \end{cases}$$

and (a) and (b) are the two different volume penalization options. It was found that both methods converged to the numerical results that do not use penalization equally as well for a flat boundary interface. Figure 4.5 shows the error of the two methods and shows the comparison of the velocity profiles in a horizontal slice of all three methods. These results are shown for $\kappa = 10$, which causes a steeper slope in the velocity as it approaches the bottom boundary and allows for better visual comparison.

It was also found the value of κ does make for a drastically different velocity profile. Figures 4.6 and 4.7 show plots of velocity and the adaptive grid for both $\kappa = 1$ and $\kappa = 10$. Additionally, as a result of the steeper slope in a higher κ value, there is a finer resolution near the penalization zone.

Figure 4.5 shows that the slopes of velocity along the vertical direction in the penalized case are not exactly equivalent to the non-penalized case. Further investigation has begun to see if this solution will converge to the non-penalized solution as the penalization parameter, η_{pen} is decreased. A preliminary study has been done and is shown in Figure 4.8. Although, the convergence is not as good as the no slip Brinkman penalization, it still may be more than sufficient.

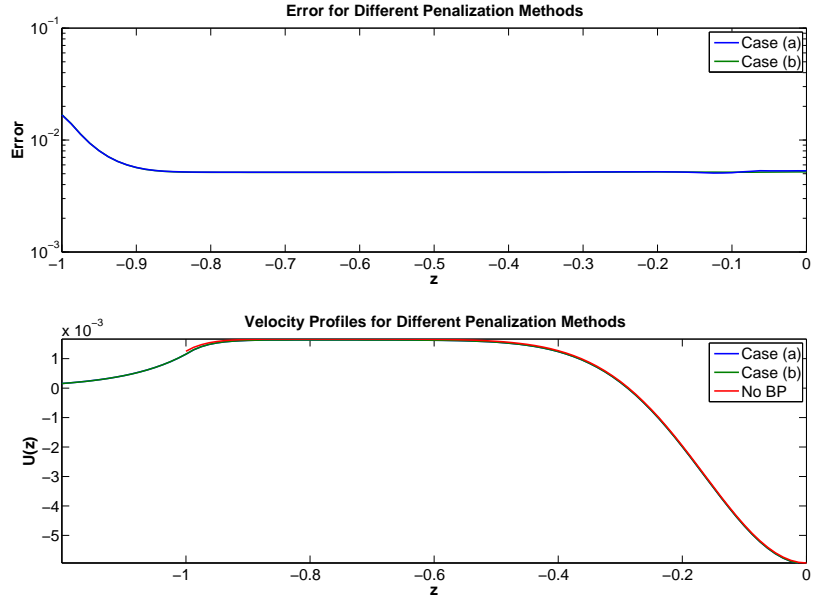


Figure 4.5: Top: the error of the two penalization methods (a) and (b) computed against numerical results from non-penalized implementation of slip boundary conditions. Bottom: the velocity profiles of all three methods (two penalization method and non-penalized approach for a slice at $x = 0.5$.

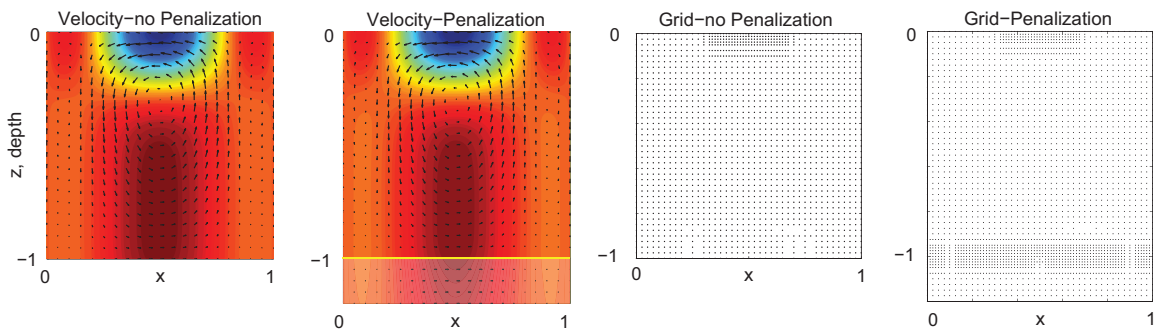


Figure 4.6: Demonstration of slip boundary conditions with and without Brinkman penalization for $\kappa = 1$.

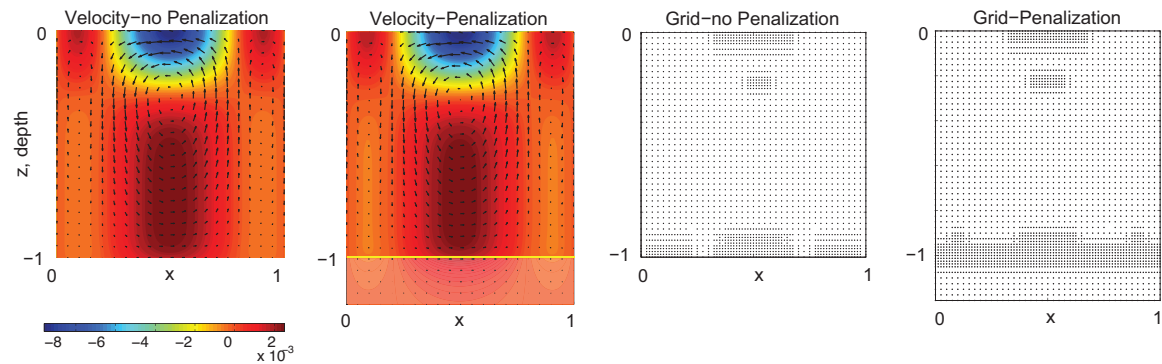


Figure 4.7: Demonstration of slip boundary conditions with and without Brinkman penalization for $\kappa = 10$.

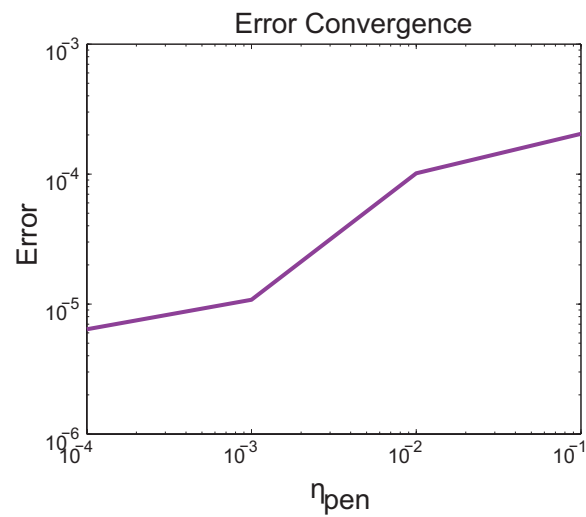


Figure 4.8: A plot of error convergence for decreasing penalization parameter for slip conditions.

Chapter 5

Non-hydrostatic Primitive Equations

For this work of developing a new approach to oceanic modeling, it was natural to start with the hydrostatic formulation of the primitive equations. The vast majority of Oceanic General Circulation Models (OGCMs) use the primitive equations under the hydrostatic pressure approximation [59]. However, due to the 3D nature of wavelets, and thus, 3D nature of the adaptive wavelet collocation method, it was found that using the non-hydrostatic form of the equations suited the numerical method much better. This is mainly due to difficulty in vertically integrating the hydrostatic pressure equation. When using a highly adaptive grid, integration in one direction is difficult and can be unstable.

The Imperial College Ocean Model (ICOM), which is a finite-element, unstructured grid model, also found that the non-hydrostatic form was more appropriate for their model, [65]. Another unstructured-grid model that uses finite-volume method is the SUNTANS model from Stanford. They also are using the non-hydrostatic form [62]. MITgcm also did some studies on hydrostatic vs. non-hydrostatic and found that the non-hydrostatic was just as computationally efficient as the hydrostatic when run in the hydrostatic limit [56]. Therefore, after working with the hydrostatic primitive equations and after confirmation from other similar oceanic models, it was decided to focus completely on the non-hydrostatic form.

5.1 Physical Model and Governing Equations

The non-hydrostatic primitive equations are the fullest version of the primitive equations used for oceanic circulation modeling. They are the Navier-Stokes equations with the effects of rotation (details in Section 2.2) and conservation of mass. Currently, stratification is also being neglected so there is no variation in density. In this model, we are using an open lid assumption, so the kinematic boundary conditions to describes the sea surface height is used.

$$\frac{\partial \eta}{\partial t} + (\mathbf{u}_h|_{z=z_{max}}) \cdot \nabla \eta = (w|_{z=z_{max}}) - \bar{w}$$

$$\frac{\partial \mathbf{u}}{\partial t} + \mathbf{u} \cdot \nabla \mathbf{u} + \frac{1}{Ro} f \hat{\mathbf{k}} \times \mathbf{u} = -\nabla P - \frac{1}{Fr^2} \hat{\mathbf{k}} + \frac{1}{Re} \nabla^2 \mathbf{u}$$

$$\nabla \cdot \mathbf{u} = 0$$

where \bar{w} is the average vertical velocity. It is subtracted off to maintain conservation of mass in an open lid system [54].

5.2 Brinkman Penalization for Non-Hydrostatic Equations

For the non-hydrostatic primitive equations, Brinkman penalization is simply a straightforward application of the incompressible Brinkman penalization [9]. It works by the addition of a forcing term in the momentum equations,

$$\frac{\partial \mathbf{u}}{\partial t} + \mathbf{u} \cdot \nabla \mathbf{u} + \frac{1}{Ro} f \hat{\mathbf{k}} \times \mathbf{u} = -\nabla P - \frac{1}{Fr^2} \hat{\mathbf{k}} + \frac{1}{Re} \nabla^2 \mathbf{u} - \frac{\chi}{\eta_{pen}} \mathbf{u}$$

where,

$$\chi(\mathbf{x}, t) = \begin{cases} 1 & \text{if } \mathbf{x} \in O(\mathbf{x}), \\ 0 & \text{otherwise} \end{cases}$$

Some preliminary tests have been done on Brinkman penalization with the non-hydrostatic form of the equations. Although, a lot of technical details still need to be shorted out regarding boundary conditions and how to deal with the surface variable, η (sea surface height). Figure 5.1 shows some of the preliminary results experimenting with Brinkman penalization on a 2D wind-driven basin case.

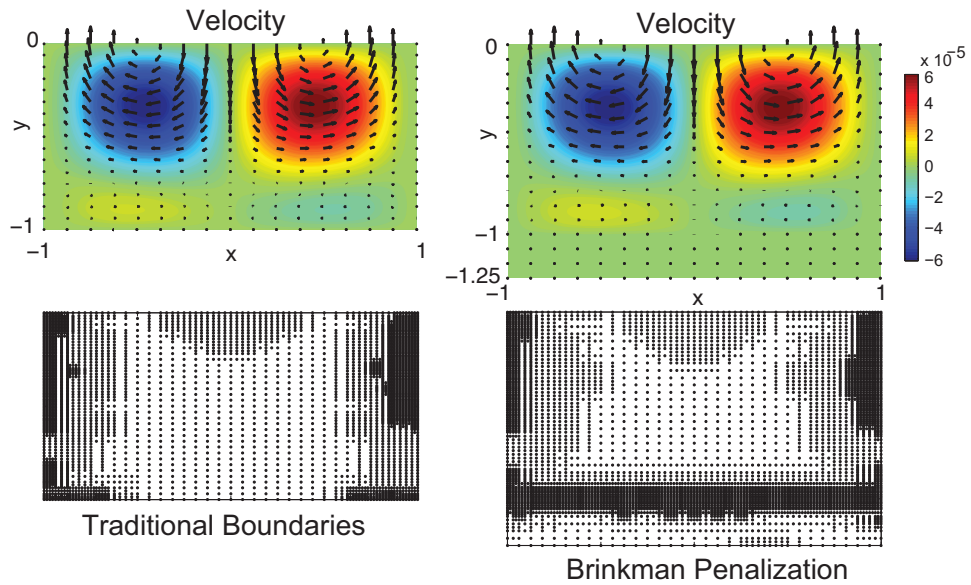


Figure 5.1: Preliminary results of the velocity and grid for non-hydrostatic form with Brinkman penalization on a 2D wind-driven basin case.

Chapter 6

Future Work

The next step for this research is to continue work with the shallow water model and the non-hydrostatic primitive equations. It can be concluded that 3D nature of wavelets and the 2D of the hydrostatic primitive equations make the hydrostatic version not work efficiently and effectively with the adaptive wavelet collocation method. Therefore, the work done on extending Brinkman penalization to slip boundary conditions will be transferred to the new non-hydrostatic model. The rest of this research will focus the shallow water model and non-hydrostatic primitive equations.

6.1 Shallow Water Model

There are two further studies to be done with adaptive wavelet shallow water model. First, high resolution basin scale studies of the shallow water equations in the North Atlantic in a rectangular domain will be run in parallel. Then, high resolution studies will be done using Brinkman penalization to describe the complex geometry of the continental topology of the North Atlantic region, also in parallel. These studies will be done in hope of providing additional information to the ocean community, as to where the Gulf Stream separates from the coast.

To complete these two studies, access to the LANL parallel computers needs to be finalized. There are also several details to work out related to the North Atlantic basin topology data and its inclusion in the wavelet code. The data that will be used for

the topology of the North Atlantic basin needs to be translated into the wavelet code's domain. Also, the module that will smooth out the topological data still needs to be finalized. The high resolution basin case is ready to run.

6.2 Non-hydrostatic Primitive Equations

There is still several details to work out with the non-hydrostatic case, mainly related to the most stable boundary conditions for the free surface and the pressure solver. Initial studies of Brinkman penalization have been done, but the treatment of the pressure in the Brinkman region needs to be closely investigated. The immediate goal is begin running in 3D with a simple wind-driven test case. Then, work will begin on adding more realistic topology and bathymetry representations. Eventually, the plan is to add stratification, more realistic wind forcing (not analytic) and a turbulence model.

Bibliography

- [1] <http://oceanservice.noaa.gov>.
- [2] <http://stommel.tamu.edu/>.
- [3] www.wikipedia.org.
- [4] Intergovernmental Panel on Climate Change (IPCC) report on climate change 2001: The scientific basis, section F.6. Technical report, 2001.
- [5] C. Hill A. Adcroft and J. Marshall. Representation of topography by shaved cells in a height coordinate ocean model. *Mon. Weather Rev.*, 125(2293-2315), 1997.
- [6] J. C. McWilliams A. F. Shchepetkin. The regional ocean modeling system: A split-explicit, free-surface, topography following coordinates ocean model. *Ocean Modeling*, 9(347-404), 2005.
- [7] A. Agarwal and P. J. Morris. Direct simulation of acoustic scattering by a rotorcraft fuselage. *AIAA Paper No. 2000-2030*, 2000.
- [8] P. Angot. Analysis of singular perturbations on the brinkman problem for fictitious domain models of viscous flows. *Mathematical Methods in the Applied Science*, 22:1395–1412, 1999.
- [9] E. Arquis and J. P. Caltagirone. Sur les conditions hydrodynamiques au voisinage d'une interface milieu fluide - milieu poreux : application à la convection naturelle. *C. R. Acad. Sci. Paris II*, 299:1–4, 1984.
- [10] M. J. Berger and M. J. Aftosmis. Aspects (and aspect ratios) of cartesian mesh methods. *Proc. 16th Int. Conf. Numer. Methods Fluid Dyn.*, 1998.
- [11] D. T. Blackstock. *Fundamentals of Physical Acoustics*. John Wiley and Sons, Inc., 2000.
- [12] A. J. H. Goddard F. Fang G. J. Gorman D. P. Marshall M. D. Eaton P. W. Power C. R. E. de Oliveira C. C. Pain, M. D. Piggott. Three-dimensional unstructured mesh ocean modelling. *Ocean Modelling*, 10(5-33), 2005.
- [13] R. C. Beardsley C. Chen, H. Liu. An unstructured grid, finite-volume, three-dimensional, primitive equations ocean model: Application to coastal ocean and estuaries. *J. Atmos. Oceanic Techno.*, 20(159-186), 2003.

- [14] D. Laurence M. Peric C. Moulinec, S. Benhamadouche. Les in a u-bend pipe meshed by polyhedral cells. Engineering Turbulence Modelling and Experiments 6, (48-60), 2005.
- [15] Vreugdenhill CB. Numerical methods for shallow water flow. Water Science and Technologies Library. Kluwer, 1994.
- [16] Iskandarani Mohamed Levin Julia Haidvogel Dale B Choi, Byoung-Ju. A spectral finite-volume method for the shallow water equations. Monthly Weather Review, 132(1777-1791), 2004.
- [17] Charles K. Chui. Wavelets: A Mathematical Tool for Signal Analysis. SIAM Monographs on Mathematical Modeling and Computation. SIAM, Philadelphia, 1997.
- [18] C. Chung. Wave propagation and scattering in computational aeroacoustics. Ph.D. dissertation, Dept. of Aerospace Engineering, Pennsylvania State University, University Park, PA, 1995, 1995.
- [19] C. Chung and P. J. Morris. Acoustic scattering from two- and three-dimensional bodies. Journal of Computational Acoustics, 6:357–375, 1998.
- [20] Peter U. Clark, Nicklas G. Pisias, Thomas F. Stocker, and Andrew J. Weaver. The role of the thermohaline circulation in abrupt climate change. Nature, 415:863–869, 2002.
- [21] D. K. Clarke, M. D. Salas, and H. A. Hassen. Euler calculations for multielement airfoils using cartesian grids. AIAA J., 24(3):353–358, 1986.
- [22] C. M. Bitz M. L. Blackmon G. B. Bonan C. S. Bretherton J. A. Carton P. Chang S. C. Doney* J. J. Hack T. B. Henderson J. T. Kiehl W. G. Large D. S. McKenna B. D. Santer* Collins, W. D. and R. D. Smith*. The community climate system model version 3 (ccsm3). Journal of Climate, 19:2122–2143, 2006.
- [23] Benoit Cushman-Roisin. Introduction to Geophysical Fluid Dynamics. 1994.
- [24] A. Beckmann D. B. Haidvogel. Numerical Ocean Circulation Modeling. 1999.
- [25] C. E. Naimie D. R. Lynch, J. T. C. Ip and F. E. Werner. Comprehensive coastal circulation model with application to gulf of maine. Cont. Shelf Res., 16(875-906), 1996.
- [26] I. Daubechies. Ten Lectures on Wavelets. Number 61 in CBMS-NSF Series in Applied Mathematics. SIAM, Philadelphia, 1992.
- [27] D. L. Donoho. Interpolating wavelet transforms. Technical Report 408, Department of Statistics, Stanford University, 1992.
- [28] L. Debreu E. Blayo. Adaptive mesh refinement for finite-difference ocean models first experiments. J. Phys. Oceanogr., 29(1239-1250), 1999.

- [29] G. R. Halliwell E. P. Chassignet, L. T. Smith and R. Bleck. North atlantic simulations with the hybrid coordinate ocean model (hycom): Impact of the vertical coordinate choice, reference pressure and thermobaricity. *J. Phys. Oceanogr.*, 33(2504-2526), 2003.
- [30] G.J. Boer W.G. Lee N.A. McFarlane D. Ramsden M.C. Reader Flato, G.M. and A.J. Weaver. The canadian centre for climate modelling and analysis global coupled model and its climate. *Clim. Dyn.*, 16:51–467, 2000.
- [31] C. C. Pain C. R. E. de Oliveira A. P. Umpleby A. J. H. Goddard G. J. Gorman, M. D. Piggott. Optimisation based bathymetry approximation through constrained unstructured mesh adaptivity. *Ocean Modelling*, 12(436-452), 2005.
- [32] T. Ezer G. L. Mellor, L.-Y. Oey. Sigma coordinate pressure gradient errors and the seamount problem. *J. Atmos. Ocean Technol.*, 15(1122-1131), 1998.
- [33] P. R. Gent. Will the north atlantic ocean thermohaline circulation weaken during the 21st century? *Geophys. Rsrch. Lett.*, 28:1023–1026, 2001.
- [34] M.R. Marinucci Giorgi, F. and G. T. Bates. Development of a second generation regional climate model (regcm2). part i boundary layer and radiative transfer processes. *Mon. Weather Rev.*, 121:2794–2813, 1993.
- [35] M.R. Marinucci-G. T. Bates Giorgi, F. and G. DeCanio. Development of a second generation regional climate model (regcm2). part ii convective processes and assimilation of lateral boundary conditions. *Mon. Weather Rev.*, 121:2814–2832, 1993.
- [36] D. Goldstein, R. Handler, and L. Sirovich. Modeling a no-slip flow boundary with an external force field. *J. Comput. Phys.*, 105:354–366, 1993.
- [37] C. Cooper-C.A. Senior H.T. Banks J.M. Gregory T.C. Johns J.F.B. Mitchell Gordon, C. and R.A. Wood. The simulation of sst, sea ice extents and ocean heat transports in a version of the hadley centre coupled model without flux adjustments. *Clim. Dyn.*, 16:147–168, 2000.
- [38] S. M. Griffies. *Fundamentals of Ocean Models*. 2004.
- [39] K. Morgan J. Peraire. Unstructured mesh generation including directional refinement for aerodynamic flow simulation. *Finite Elem. Anal. Des.*, 25(343-356), 1997.
- [40] R.E. Carnell-J.F. Crossley J.M. Gregory J.F.B. Mitchell C.A. Senior S.F.B. Tett Johns, T.C. and R.A. Wood. The second hadley centre coupled ocean-atmosphere gcm: model description, spinup and validation. *Clim. Dyn.*, 13:103–134, 1997.
- [41] N. Kevlahan and J.-M. Ghidaglia. Computation of turbulent flow past an array of cylinders using a spectral method with Brinkman penalization. *Eur. J. Mech./B*, 2001. To appear.
- [42] N. K.-R. Kevlahan and O. V. Vasilyev. An adaptive wavelet collocation method for fluid-structure interaction at high Reynolds numbers. *SIAM J. Sc. Comp.*, 26(6):1894–1915, 2005.

- [43] N. K.-R. Kevlahan, O. V. Vasilyev, and A. Cherhabili. An adaptive wavelet method for turbulence in complex geometries. In M. Deville and R. Owens, editors, 16th Imacs World Congress 2000, Proceedings, Lausanne - August 21-25, 2000, volume 411-39. IMACS, 2000.
- [44] B. Barnier L. Debreu, E. Blayo. A general adaptive multi-resolution approach to ocean modelling: Experiments in a primitive equation model of the north atlantic. Adaptive Mesh Refinement - Theory and Applications. Proceedings of the Chicago Workshop on Adaptive Mesh Refinement Methods, Sept. 3-5, 2003, (303-313), 2005.
- [45] P. Luong L. N. Ly. Numerical multi-block grids in ocean circulation modeling. Appl. Math. Model., 23(865-879), 1999.
- [46] M. C. Lai and C. S. Peskin. An immersed boundary method with formal second order accuracy and reduced numerical viscosity. J. Comput. Phys., 160:705–719, 2000.
- [47] O. A. Laik and P. J. Morris. Direct simulation of acoustic scattering by two- and three-dimensional bodies. Journal of Aircraft, 37:68–75, 2000.
- [48] J. Liandrat and Ph. Tchamitchian. Resolution of the 1d regularized Burgers equation using a spatial wavelet approximation. Technical report, NASA Contractor Report 187480, ICASE Report 90-83, NASA Langley Research Center, Hampton VA 23665-5225, 1990.
- [49] C. C. Pain P. A. Allison A. S. Candy B. T. Martin M. R. Wells M. D. Piggott, G. J. Gormon. A new computational framework for multi-scale ocean modelling based on adapting unstructured meshes. Int. J. Numer. Methods Fluids, 56(1003-1015), 2008.
- [50] G. J. Gormon P. W. Power A. J. H. Goddard M. D. Piggott, C. C. Pain. h, r, and hr adaptivity with applications in numerical ocean modelling. Ocean Modelling, 10(95-113), 2005.
- [51] D.B. Haidvogel M. Iskandarani and J. Levin. A three-dimensional spectral element model for the solution of the hydrostatic primitive equations. Journal of Computational Physics, 2(361-705), 2003.
- [52] L. Mortier M. Laugier, P. Agnot. Nested grid methods for an ocean model a comparative study. Int. J. Numer. Methods Fluids, 23(1163-1195), 1996.
- [53] S. Mallat. A Wavelet Tour of Signal Processing. Academic Press, 1998.
- [54] A. Adcroft C. Hill L. Perelman Marshall, J. and C. Heisey. A finite-volume, incompressible navier stokes model for studies of the ocean on parallel computers. J. Geophysical Res., 102(C3):5753–5766, 1997.
- [55] C. Hill L. Perelman Marshall, J. and A. Adcroft. Hydrostatic, quasi-hydrostatic, and nonhydrostatic ocean modeling. J. Geophysical Res., 102(C3):5733–5752, 1997.
- [56] Jones H. Marshall, J. and C. Hill. Efficient ocean modeling using non-hydrostatic algorithms. Journal of Marine Systems, 18:115–134, 1998.

- [57] Gerard J. Gorman David P. Marshall Peter D. Killworth Matthew D. Piggott, Christopher C. Pain. Unstructured adaptive meshes for ocean modeling. Ocean Modeling in an Eddying REgime Geophysical Monograph Series 177, (383-408), 2008.
- [58] D. J. Mavriplis. Accurate multigrid solution of the euler equations on unstructured and adaptive meshes. AIAA J., 28:213–221, 1990.
- [59] J. C. McWilliams. Modeling the oceanic general circulation. Annual Review of Fluid Mechanics, 1996.
- [60] R. Mittal and G. Iaccarino. Immersed boundary methods. Annu. Rev. Fluid Mech., 37:239–261, 2005.
- [61] Oleg Vasilyev Nicholas Kevlahan. An adaptive wavelet collocation method for fluid-structure interaction at high reynolds numbers. SIAM Journal of Scientific Computing, 2005.
- [62] R. L Street O. B. Fringer, M. Gerritsen. An unstructured-grid, finite-volume, nonhydrostatic, parallel coastal ocean simulator. Ocean Modelling, 14(139-173), 2006.
- [63] J. Z. Zhu P. Nithiarasu O.C. Zienkiewicz, R. L. Taylor. The Finite Element Method: Its Basis and Fundamentals; for Solid and Structural Mechanics; for Fluid Mechanics. 2005.
- [64] P. Fabrie P. Angot, C-H Bruneau. A penalization method to take into account obstacles in viscous flows. Numerische Mathematik, 81(497-520), 1999.
- [65] V. Legat E. Deleersnijder J. F. Remacle P. E. Bernard, N. Chevaugeon. High-order h-adaptive discontinuous galerkin methods for ocean modeling. Ocean Dyn., 9(03497), 2007.
- [66] C. S. Peskin. Flow patterns around heart valves: a digital computer method for solving the equations of motion. Ph.D. Thesis, Albert Einstein College of Medicine, 1972, 1972.
- [67] C. S. Peskin. The immersed boundary method. Acta Numerica, pages 479–517, 2002.
- [68] M.L. Gallani P.R. Rowntree Pope, V. and R.A. Stratton. The impact of new physical parameterizations in the hadley centre climate model: Hadam3. Clim. Dyn., 16:123–146, 2000.
- [69] J. W. Purvis and J. E. Burkhalter. Prediction of critical mach number for store configurations. AIAA J., 17(11):1170–1177, 1979.
- [70] Oleg V. Vasilyev Qianlong Liu. A brinkman penalization method for compressible flow in complex geometries. Elseview Science, 2006.

- [71] M. D. Piggott A. J. H. Goddard C. R. E de Oliveira R. Ford, C. C. Pain and A. P. Umpleby. A nonhydrostatic finite-element model for three-dimensional stratified oceanic flows. part i: Model formulation. *American Meteorological Society*, 132(2816-2831), 2004.
- [72] Li X Shephard MS Remacle J-F, Soares Frazao. An adaptive discretization of shallow-water equations based on discontinuous galerkin methods. *Int J Numer Methods Fluids*, 52:903–923, 2006.
- [73] K. Arpe L. Bengtsson M. Christoph M. Claussen L. Dmenil M. Esch M. Giorgetta U. Schlese Roeckner, E. and U. Schulzweida. The atmospheric general circulation model echam-4: model description and simulation of present-day climate. *Max-Planck Institute for Meteorology, Report No.218, Hamburg, Germany*, page 90 pp, 1996.
- [74] G. Kivman S. Danilov and J. Schroter. A finite element ocean model: Principles and evaluation. *Ocean Model.*, 6(125-150), 2004.
- [75] F. O. Bryan E. P. Chassignet R. Gerdes H. Hasumi A. Hirst A.M. Treguier D. Webb S. m. Griffies, C. Boning. Developments in ocean climate modelling. *Ocean Model.*, 2(123-192), 2000.
- [76] G. Rickard S. Popinet. A tree-based solver for adaptive ocean modelling. *Ocean Model.*, 16(224-249), 2007.
- [77] E. M. Saiki and S. Biringen. Numerical simulation of a cylinder in uniform flow: application of a virtual boundary method. *J. Comput. Phys.*, 123:450–465, 1996.
- [78] R. D. Smith, M. O. Maltrud, F. O. Bryan, and M. W. Hecht. Numerical simulation of the north atlantic ocean at $1/10^\circ$. *J. Phys. Ocean.*, 30:1532–1561, 2000.
- [79] Zech Y Soares Frazao S. Dam-break in channels with 90 degree bend. *J. Hydraul Res, American Society of Civil Engineers*, 128:956–968, 2002b.
- [80] W. Sweldens. The lifting scheme: A construction of second generation wavelets. *SIAM J. Math. Anal.*, 29(2):511–546, 1998.
- [81] J. F. Thompson, Z. U. A. Warsi, and C. W. Mastin. Boundary fitted coordinate systems for numerical solution of partial differential equations – a review. *J. Comput. Phys.*, 47:1–108, 1982.
- [82] Y. H. Tseng and J. H. Ferziger. A ghost-cell immersed boundary method for flow in complex geometry. *J. Comput. Phys.*, 192:593–623, 2003.
- [83] O. V. Vasilyev. Solving multi-dimensional evolution problems with localized structures using second generation wavelets. *Int. J. Comp. Fluid Dyn., Special issue on High-resolution methods in Computational Fluid Dynamics*, 17(2):151–168, 2003.
- [84] O. V. Vasilyev. Solving multi-dimensional evolution problems with localized structures using second generation wavelets. *Int. J. Comp. Fluid Dyn., Special issue on High-resolution methods in Computational Fluid Dynamics*, 17(2):151–168, 2003.

- [85] O. V. Vasilyev and C. Bowman. Second generation wavelet collocation method for the solution of partial differential equations. *J. Comp. Phys.*, 165:660–693, 2000.
- [86] O. V. Vasilyev and C. Bowman. Second generation wavelet collocation method for the solution of partial differential equations. *J. Comp. Phys.*, 165:660–693, 2000.
- [87] O. V. Vasilyev and N. K.-R. Kevlahan. Hybrid wavelet collocation - Brinkman penalization method for complex geometry flows. *Int. J. Numerical Methods in Fluids*, 40:531–538, 2002.
- [88] O. V. Vasilyev and S. Paolucci. A dynamically adaptive multilevel wavelet collocation method for solving partial differential equations in a finite domain. *J. Comput. Phys.*, 125:498–512, 1996.
- [89] O. V. Vasilyev and S. Paolucci. A fast adaptive wavelet collocation algorithm for multi-dimensional PDEs. *J. Comput. Phys.*, 138:16–56, 1997.
- [90] L. White. Accuracy and consistency in finite element ocean modeling. *PhD Thesis*, 2007.
- [91] R. A. Wood, A. B. Keen, J. F. B. Mitchell, and J. M. Gregory. Changing spatial structure of the thermohaline circulation in response to atmospheric CO_2 forcing in a climate model. *Nature*, 399:572–575, 1999.
- [92] D. D. Zeeuw and K. G. Powell. An adaptively refined cartesian mesh solver for the euler equations. *J. Comput. Phys.*, 104:56–68, 1993.